The MFN2 Q367H variant reveals a novel pathomechanism connected to mtDNA-mediated inflammation.

Mashiat Zaman[1], Govinda Sharma[2*], Walaa Almutawa[2*], Tyler GB Soule[3], Rasha Sabouny[2], Matt Joel[3], Armaan Mohan[2], Cole Chute[2], Jeffrey T Joseph[4], Gerald Pfeffer[5#], Timothy E. Shutt[6#]

[1]Department of Biochemistry & Molecular Biology, Cumming School of Medicine, Hotchkiss Brain Institute, University of Calgary

[2]Department of Biochemistry & Molecular Biology, Cumming School of Medicine, University of Calgary

[3]Department of Neuroscience, Cumming School of Medicine, Hotchkiss Brain Institute, University of Calgary

[4]Hotchkiss Brain Institute, Department of Clinical Neurosciences, Department of Pathology, Cumming School of Medicine, University of Calgary

[5]Hotchkiss Brain Institute, Department of Clinical Neurosciences; and Alberta Child Health Research Institute, Department of Medical Genetics, Cumming School of Medicine, University of Calgary

[6]Departments of Medical Genetics and Biochemistry & Molecular Biology, Cumming School of Medicine, Hotchkiss Brain Institute, Snyder Institute for Chronic Diseases, Alberta Children's Hospital Research Institute; University of Calgary

*Equal contribution

[#]Corresponding authors

Abstract

Pathogenic variants in the mitochondrial protein MFN2 are typically associated with a peripheral neuropathy phenotype, but can also include a variety of additional pathologies including myopathy. Here, we identified a previously uncharacterized MFN2 variant, Q367H, in a patient diagnosed with late-onset distal myopathy, but without peripheral neuropathy. Consistent with the hypothesis that the Q367H MFN2 variant contributes to the patient's pathology, patient fibroblasts and transdifferentiated myoblasts showed changes consistent with impairment of several MFN2 functions. We also observed mtDNA outside of the mitochondrial network that co-localized with early-endosomes, and measured activation of both TLR9 and cGAS-STING inflammation pathways that sense mtDNA. Notably, the inflammatory signaling was increased 3-10 fold in transdifferentiated patient myoblasts. We also found that re-expressing the Q367H variant in MFN2 knockout cells also induces mtDNA release. As elevated inflammation can cause myopathy, our findings linking the Q367H MFN2 variant with elevated TLR9 and cGAS-STING signaling that is exacerbated in myoblasts, can explain patient's myopathy. Thus, we characterize a novel MFN2 variant in a patient with an atypical presentation that separates peripheral neuropathy and myopathy phenotypes, and establish a potential novel pathomechanism connecting MFN2 dysfunction to mtDNA-mediated inflammation.

37 **Introduction**

38 Mitochondria are highly dynamic cellular structures that fuse, divide, move about the cell, and
39 interact with other organelles. The integral outer-mitochondrial-membrane (OMM) proteins Mitofusin1
40 (MFN1) and Mitofusin 2 (MFN2) mediate fusion of the outer mitochondrial membrane. MFN2, though
41 named for its role in mitochondrial fusion, is also actively involved in several other dynamic processes
42 (1): it mediates contacts between mitochondria and the endoplasmic reticulum (ER) (2), referred to here
43 as mito-ER contact sites (MERCs); is involved in mitochondrial interactions with lipid droplets (3), early
44 endosomes (4), and the nucleus (5); and also plays an active role in mitochondrial autophagy
45 (mitophagy) (6,7).

46 Impairments in mitochondrial dynamics are linked to genetic neuropathies, with pathogenic
47 variants in MFN2 are typically associated with the axonal peripheral neuropathy Charcot-Marie-Tooth
48 disease subtype 2A (CMT2A)(8). Characterized by weakness, numbness and pain in the distal regions of
49 the body, CMT2A is often an early-onset progressively-worsening disease (9). In addition to peripheral
50 neuropathy, patients with certain MFN2 variants can present with other pathogenic phenotypes, such as
51 myopathy (10–12), optic atrophy, sensorineural hearing loss, ataxia (13), or multiple symmetric
52 lipomatosis (MSL) (14–16). How and why different variants in MFN2 lead mechanistically to pathology is
53 not fully understood, though it is likely not as simple as reduced mitochondrial fusion (17).

54 In addition to its critical role in neurons, MFN2 is also important for muscle function. Muscle-
55 specific MFN2 knockout (KO) results in muscle atrophy, which is attributed to loss of mitochondrial
56 fusion and subsequent instability of the mitochondrial genome (mtDNA) (18). On top of the depletion of
57 mtDNA copy number that is thought to contribute to respiratory deficiency, mtDNA can accumulate
58 point mutations and deletions in the muscle tissue of these KO mice. A role for MFN2 in maintaining
59 mtDNA is further supported by the fact that certain pathogenic *MFN2* variants show a reduction in
60 mtDNA copy number (19,20) or lead to mtDNA deletions (21). However, highlighting our incomplete
61 understanding of the pathology caused by MFN2 deficiency and the role played by mtDNA, not all
62 pathogenic *MFN2* variants impair mitochondrial fusion, impact mtDNA, or cause respiratory deficiency
63 (17).

64 Beyond its role of encoding OXPHOS proteins, mtDNA is now also recognized to play an
65 important role as an inflammatory signalling molecule when released from mitochondria (22,23).
66 Examples of inflammatory signalling pathways that detect mtDNA-mediated include TLR9 (4,19), cGAS-
67 STING (24,25) and the inflammasome (26,27). Notably, a recent study showed that inducible muscle-
68 specific loss of MFN1 causes mtDNA release via early endosomes, leading to activation of TLR9/NF-kB

69 inflammation and myopathy (4). Importantly, pharmacological inhibition of this inflammation improved
70 the muscle atrophy and physical performance in these mice, implicating sterile inflammation in the
71 muscle pathology of these mice. Nevertheless, the role of mtDNA-mediated inflammation in the
72 pathology of pathogenic *MFN2* variants has not been described to date.
73 Here we report a novel MFN2 variant, Q367H, in a patient diagnosed with late onset distal
74 myopathy. Functional characterization of patient fibroblasts, transdifferentiated myoblasts and a KO re-
75 expression cell model reveals mtDNA-mediated inflammation likely explain the patient myopathy, thus
76 expanding our understanding of the mechanisms by which MFN2 dysfunction contributes to pathology.
77
78
79 **Methods**
80 Ethics statement
81 The patient provided written informed consent for participation in research and consented to
82 the publication of this report. He was provided with a copy of the draft article prior to submission.
83 Genetic sequencing and human tissue studies with this participant were part of research protocols
84 (REB15-2763 and REB17-0850) approved by the Conjoint Health Research Ethics Board at the University
85 of Calgary.
86
87 Exome Sequencing, Variant Confirmation and Sequence Conservation Study
88 DNA was extracted from blood collected into EDTA tubes using standard protocols. Library
89 preparation proceeded using the Ion Ampliseq Exome RDY Panel (Thermo Fisher, A38264) according to
90 manufacturer's protocol. Automated chip loading and templating used the Ion Chef system and 540
91 chip/chef kit (Thermo Fisher, A30011), and sequencing was performed on an Ion S5 system (Thermo
92 Fisher, A27212), according to manufacturer's protocols. Base calling, read alignment to hg19, coverage
93 analysis, and variant calling were performed with Torrent Suite (v. 5.10.1; Thermo Fisher). Similar
94 analysis can be performed using an alternative bioinformatic pipeline as described previously (28).
95 Patient VCFs were annotated for predicted variant consequence, gnomAD allele frequency, CADD score,
96 and OMIM phenotypes, in addition to default parameters with Ensembl's command line Variant Effect
97 Predictor (VEP). We additionally aligned off-target reads from exome sequencing to identify any mtDNA
98 variants, as previously described (29).
99 The variant was verified by Sanger sequencing. Briefly, total genomic DNA was collected using
100 the E.Z.N.A Tissue DNA Extraction Kit (VWR, CA101319-018). The region of interest was amplified using

101 PCR with the following primers (F-GAGAAGAGCAGAGAGGCTCTTG and R-ACACAGGGAATCGTGCTGC).
102 Subsequently the amplified region was sequenced by Sanger sequencing at University of Calgary Centre
103 For Health Genomics And Informatics.
104 Amino acid sequence alignment was performed using the T-COFFEE online tool (30). The
105 sequences were collected from UniProt(31). The following accession codes were used for the sequences:
106 MFN2: O95140-1, MFN1: Q8IWA4, Mouse MFN2: Q80U63, Fish MFN2: A8WIN6, Chicken MFN2: E1BSH7,
107 Frog MFN2: Q28CS2, Fruit fly MFN: Q7YU24, Worm MFN: Q23424.
108
109 Quantification of Protein Amounts:
110 Relative quantities were measured using Western Blot Analysis, as previously described (13).
111 Briefly, cells were lysed with Pierce RIPA buffer (Thermo Scientific™, 89900), and subsequently total
112 protein was quantified by a BCA assay. 50 µg of protein was loaded from control and patient fibroblasts
113 on to an SDS-PAGE gel. After running the gel, the blots were transferred to a PVDF membrane overnight.
114 The blots were probed using the following antibodies: anti-MFN2 (Abnova, H00009927-M03; 1:1000),
115 anti-MFN1 (Cell Signaling Technology, D6E2S; 1:1000), anti-OPA1 (BD Transduction Laboratories, 612607;
116 1:1000), anti-Actin (Sigma, A5316; 1:1000). Secondary antibodies complimentary to the primary host
117 species were used- goat anti-rabbit IgG, HRP linked Antibody (Cell Signaling Technology, 7074S) or goat
118 anti-mouse IgG-HRP (Santa Cruz Biotechnology, sc-2055). The membranes were visualized with
119 SuperSignal™ West Femto Maximum Sensitivity Substrate (Thermo Scientific™, 34095) using the Bio-Rad
120 ChemiDoc Imaging System. Bands were quantified using Fiji (32).
121
122 Cell Culture and Maintenance
123 Fibroblasts from the patient and healthy individual (age and sex-matched) were generated
124 through skin biopsies as described (28). The cells were cultured using Minimum Essential Media (Gibco,
125 11095080), supplemented with 10% Fetal Bovine Serum and 1mM Sodium Pyruvate. Glucose-free
126 conditions were established using DMEM No Glucose media (Gibco, 11966025), supplemented with
127 5mM galactose, 10% FBS and 1mM Sodium Pyruvate. Cells were grown in an incubator, maintained at
128 37°C and 5% CO_2. For the fatty acid pulse-chase assay, the cells were grown in the glucose media
129 mentioned above, or glucose-free media with 10% FBS, but no galactose.
130 WT U2OS and U2OS MFN2 KO cells, a gift from Dr. Edward A Fon (7) (McGill University, Canada),
131 were grown in DMEM High Glucose Media (Gibco, 11965118) supplemented with 10% FBS. A retrovirus
132 plasmid containing the MFN2 open reading frame followed by an internal ribosomal entry site and

133 mitochondria-targeted mNeonGreen was constructed through VectorBuilder (VB230626-1399nzw). A
134 version of the plasmid with the Q367H variant was generated using in-fusion mutagenesis (Takarabio,
135 638951). Retrovirus was generated by transfecting Phoenix cells with WT or Q367H plasmids using
136 Lipofectamine 3000 transfection (ThermoFisher, L3000015). U2OS MFN2 KO cells were then transduced
137 with retrovirus and cells were sorted for mNeonGreen fluorescence using fluorescence activated cell
138 sorting (Sony SH800). Endogenous levels of MFN2 expression was confirmed by immunoblotting, and
139 these stable lines re-expressing either WT MFN2 or the Q367H variant were used for subsequent
140 analysis.
141
142 Mitochondrial Morphology Analysis
143 Mitochondrial morphology was analyzed by immunostaining as described previously (33), where
144 30,000 cells were grown in 12mm coverslips for 24 hours and subsequently fixed by 4% PFA for 20
145 minutes at 37°C. Cells were permeabilized using 0.1% Triton X-100 (MP Biomedicals, J00105) and
146 blocked using 5% FBS. The OMM protein TOMM20 was chosen to visualize the mitochondrial network,
147 where cells were incubated with mouse anti-TOMM20 (Santa Cruz Biotechnology, F-10, RRID:
148 AB_628381) overnight, the subsequently probed with goat anti-mouse secondary conjugated with Alexa
149 fluor 488 (Thermo Fisher Scientific, A-11029). Cover slips were then mounted on glass slides using
150 ProLong Diamond Antifade Mountant with DAPI (Invitrogen, P36966).
151
152 Oxygen Consumption Rate
153 The cellular oxygen consumption rate assay for control and patient fibroblasts was performed as
154 previously described (34). Briefly, 40,000 cells were seeded in wells of the XF-24 plates (Agilent). The
155 media on the plates was replaced 24 hours later with Seahorse CF Base Medium, supplemented with
156 1mM Pyruvate, 2mM Glutamine and 10mM Glucose and brought to pH 7.4. Post-incubation for 45
157 minutes with CO_2, cells were loaded into the Seahorse XF24 Analyzer. Oxygen consumption rates were
158 measured at three time points, following administration of Oligomycin (0.5 µM), Carbonyl cyanide-p-
159 trifluoromethoxyphenylhydrazone (FCCP) (1 µM) and Antimycin A (0.5 µM). Following the experiment,
160 cells in each well were lysed with Pierce RIPA buffer and total protein for each well was quantified with
161 BCA assays, for normalization purposes.
162
163 Measurement of mitochondrial membrane potential:

164 Fibroblasts were stained with 400 nM TMRE (Sigma-Aldrich, 87917) for 40 minutes, prior to
165 trypsinization. Cells were then stained using LIVE/DEADTM Fixable Violet Dead Cell Stain kit (Invitrogen,
166 L34964) re-suspended in PBS prior to acquisition on the cytometer. The cell fluorescence was measured
167 using a Becton-Dickson FACS CANTO cytometer supported by the BD FACS Diva software (BD Biosciences,
168 Franklin Lakes, NJ). TMRE signal was detected by a 488 nM laser with a PE-detector, and live/dead signal
169 was detected by a 405 nM laser with a BV421 detector. Dead cells and doublets were excluded from
170 analysis. Mitochondrial membrane potential was reported as mean fluorescent intensity (MFI) values of
171 live, single cells analyzed using Flow-Jo analysis software.
172
173 mtDNA and Mitochondrial Nucleoid Analyses
174 Mitochondrial nucleoids were visualized using confocal microscopy as previously reported (35).
175 Briefly, 30,000 control and patient fibroblasts were grown on coverslips for 24 hours and fixed with 4%
176 PFA. Cells were permeabilized with 0.2% Triton X-100 and blocked with 5% FBS. Mitochondrial nucleoids
177 were labelled using mouse anti-dsDNA antibody (Developmental Studies Hybridoma Bank,
178 AB_10805293, RRID:AB_10805293) and subsequently visualized using the goat anti-mouse secondary
179 conjugated with Alexa fluor 488. The mitochondrial network was also labelled using anti-rabbit TOMM20
180 rabbit anti-TOMM20 (Abcam, ab186735), which was visualized with anti-Rabbit secondary conjugated
181 with Alexa fluor 647 (Thermo Fisher Scientific, A-21245). Cover slips were mounted using ProLong
182 Diamond Antifade Mountant with DAPI.
183 mtDNA copy number analysis was performed using qPCR. Total DNA was collected from control
184 and patient fibroblasts seeded at the same density. Relative mtDNA copy number was analyzed using
185 nuclear-encoded housekeeping gene 18S, by amplification using the following primers:
186 mito-F- CACCCAAGAACAGGGTTTGT
187 mito-R- TGGCCATGGGTATGTTGTTAA
188 18S-F- TAGAGGGACAAGTGGCGTTC
189 18S-R- CGCTGAGCCAGTCAGTGT
190 For qPCR, 50ng of total DNA was loaded into each well a 96-well plate and the reaction was
191 performed using the QuantStudio6 Flex Real-Time PCR system (Thermo Fisher Scientific). The delta Ct
192 method was used to determine the relative copy number.
193 Long range PCR was done to look for mtDNA deletions using the Takara LA Taq Polymerase
194 (Takara Bio, RR002M). Total DNA was collected from control and patient fibroblasts and 16.2kBP
195 fragment was amplified using the following primers- (F- ACCGCCCGTCACCCTCCTCAAGTATACTTCAAAGG

196 and R- ACCGCCAGGTCCTTTGAGTTTTAAGCTGTGGCTCG). Long Range PCR was done using the following
197 conditions- (94 °C for 1 min; 98 °C for 10 s, and 68 °C for 11 min (30 cycles), followed by a final extension
198 cycle at 72 °C for 10 min). The products following the reaction were visualized by gel electrophoresis on a
199 0.6% gel run for 18 hours at 18V.
200
201
202 Mito-ER Contact Sites
203 The proximity ligation assay was used to look for MERCs, using the Duolink In Situ Detection kit
204 (Sigma Aldrich, DUI92008). Briefly, 30,000 control and patient cells were grown on coverslips for 24
205 hours and subsequently fixed using 4%PFA. Cells were permeabilized with 0.1% Triton X-100 and blocked
206 using the blocking reagent provided by the kit. The cells were then incubated overnight using mouse-
207 anti-Calnexin (Sigma-Aldrich, MAB3126) and rabbit anti-TOMM20 (Abcam, ab186735). Following
208 incubation, PLA probes, complementary to the primary antibodies, anti-mouse (Sigma-aldrich,
209 DUO92004) and anti-rabbit (Sigma-aldrich, DUO92002) were added to the coverslips. The addition of
210 DNA ligase and DNA polymerase were subsequently carried out using manufacturer's instructions and
211 using the reagents provided in the kit. Finally, secondary antibodies anti-mouse secondary conjugated
212 with Alexa fluor 488 (Thermo Fisher Scientific, A-11029) and anti-Rabbit secondary conjugated with
213 Alexa fluor 647 (Thermo Fisher Scientific, A-21245) were added for visualizing the ER and mitochondrial
214 networks respectively. The coverslips were mounted with ProLong Diamond Antifade with DAPI before
215 imaging.
216
217 Lipid Droplets and Fatty Acid Pulse-Chase
218 Total cellular lipid droplets were labelled using HCS LipidTox Green (Thermo Fisher Scientific,
219 H34350), following the same immunostaining protocol to label the mitochondrial network, except for
220 using 0.1% Saponin (Sigma Aldrich, SAE0073-10G) as the permeabilizing solution. The mitochondrial
221 network was also labelled using anti-rabbit TOMM20 rabbit anti-TOMM20 (Abcam, ab186735), which
222 was visualized with anti-Rabbit secondary conjugated with Alexa fluor 647 (Thermo Fisher Scientific, A-
223 21245).
224 For the fatty acid pulse-chase assay, 50,000 cells were seeded on a 35mm glass bottom dish with
225 20mm indented imaging region. Cells were grown for 24 hours, after which they were pulsed with the
226 fluorescent fatty acid precursor BODIPY 558/568 C_{12} (Invitrogen, D3835). After 24 hours incubation with
227 the BODIPY, cells were incubated with either glucose or glucose-free media and chased at time points 0

228 hours, 6 hours and 24 hours following the addition of the two media conditions. When the variable
229 media conditions were added, MitoTracker Green (Invitrogen, M7514) was also added at 50nM
230 concentration for visualizing the mitochondrial network.
231
232 Mitochondria, mtDNA and Early Endosome Imaging
233 The triple staining of the mitochondrial network, mtDNA and early endosomes was performed
234 using sequential immunostaining. The steps until blocking are the same as described above for the
235 mitochondrial network. Following blocking, primary antibodies were added for the mtDNA (same as
236 above) and mitochondrial network (same as above) and secondary antibodies were added accordingly-
237 anti-mouse secondary conjugated with Alexa fluor 488 (Thermo Fisher Scientific, A-11029) and anti-
238 Rabbit secondary conjugated with Alexa fluor 568 (Thermo Fisher Scientific, A-11004). Following
239 secondary antibody incubation, coverslips were thoroughly washed with PBS and the primary antibody
240 to label early endosomes was added rabbit anti-RAB5 (Cell Signaling Technology, 3547T). Subsequently,
241 the complementary secondary antibody anti-Rabbit secondary conjugated with Alexa fluor 647 (Thermo
242 Fisher Scientific, A-21245) was added. The coverslips were mounted using ProLong Diamond Antifade
243 mounting media.
244
245 Fibroblast Transdifferentiation
246 The coding sequence for human myoD1 (accession NM_002478) was PCR amplified from a
247 human skeletal muscle cDNA library and subcloned into pWPXL (pWPXL was a gift from Didier Trono
248 (Addgene plasmid # 12257) in place of eGFP at the 5'BamHI and 3'EcoRI restriction sites. The DNA
249 sequence was confirmed using Sanger DNA sequencing.
250 Lentivirus production was performed using 293FT cells grown to 90% confluency on five, 15 cm^2
251 cell culture plates, by cotransfecting 112.5 µg pWPXL-myoD1, 73 µg psPAX2 and 39.5 µg pMD2.G [gifts
252 from Didier Trono (Addgene, plasmid # 12260) using PEIpro transfection reagent (Polyplus). The cell
253 culture media was collected 48 hours post-transfection, quantified using Lenti-X™ GoStix™ Plus (Takara
254 Bio USA, 631280), centrifuged at 500xg for 5 min, 0.45 um filtered and stored at -80°C as 5 mL aliquots.
255 Non-immortalized primary fibroblasts below passage 5 were grown at 37°C, 5% CO_2 in complete
256 media: DMEM – high glucose (Corning, 10-013-CV), 10% FBS (Corning, 35-077-CV), 1% P/S (VWR, K952).
257 T75s or 24 well plates were coated in 0.1 mg/mL VitroCol Type I human collagen (Advanced BioMatrix,
258 5008) for 1 hour before gently washing with PBS. Cells were seeded at 6,300/cm^2 and transduced at 75%
259 confluency. 5 µg/mL polybrene (Sigma-Aldrich, TR-1003-G) was mixed with MYOD1 lentivus at GoStix

260 Values of either 11,500 or 12,000 depending on the biological replicate. Cells were transduced by
261 spinfection, specifically a one-hour spin at 800 xg, RT, and then lentiviral supernatant was replaced with
262 complete media. Media was changed every two days and cells were allowed to transdifferentiate for 7
263 days before fixing or RNA extraction. Conversion to myoblasts was confirmed by visualization of Desmin
264 using Desmin (D93F5) XP Rabbit mAb (CST, cat. #5332S) and secondary AlexaFluor 594 chicken anti-
265 rabbit (Invitrogen, A-21442). RNA for qPCR was extracted using RNeasy Mini Kit (QIAGEN, 74104).
266
267 Analysis of TLR9-NF-kB Signalling Pathways:
268 The expression of genes associated with the TLR9-NF-kB was analyzed by RT-qPCR. The TLR9
269 inhibitor Chloroquine (MilliporeSigma, C973P63) and the cGAS-STING inhibitor Ru.521 (Aobious,
270 AOB37877) were added to the cell culture media (final concentration 1uM) for 24 hours, and
271 subsequently the cells were washed five times with PBS. Briefly, total RNA was extracted from cells using
272 the HP Total RNA Extraction Kit (VWR, CA101414-852), according to the manufacturer's instructions. The
273 collected RNA was reverse transcribed using the iScript Advanced cDNA Synthesis Kit (BioRad, 1725038).
274 Subsequently, qPCR was performed using the QuantStudio 6 Real-Time PCR system (Thermo Scientific).
275 The primers used for amplification of target genes are:
276 Beta Actin- F- AAGACCTGTACGCCAACACA
277 Beta Actin- R- AGTACTTGCGCTCAGGAGGA
278 Asc-F- CATGAACTGATCGACAGGATG
279 Asc-R- GGACCTCCTCCAAATGTTTC
280 IL6-F-- AGACAGCCACTCACCTCTTCAG
281 IL6-R- TTCTGCCAGTGCCTCTTTGCTG
282 Nlrp3-F- GCTGGCATCTGGATGAGGAA
283 Nlrp3-R- GTGTGTCCTGAGCCATGGAA
284 S100a9-F- GGAATTCAAAGAGCTGGTGC
285 S100a9-R- TCAGCATGATGAACTCCTCG
286 TNF-F- GCCCATGTTGTAGCAAACCC
287 TNF-R- GGAGGTTGACCTTGGTCTGG
288 IFN-α-F- AAATACAGCCCTTGTGCCTGG
289 IFN-α-R- GGTGAGCTGGCATACGAATCA
290 IFN-β-F- AAGGCCAAGGAGTACAGTC
291 IFN-β-R- ATCTTCAGTTTCGGAGGTAA

292

293 Imaging and Analyses

294 All imaging was performed as previously described (24). The Olympus Spinning Disk Confocal
295 System (Olympus SD OSR) was used with the UAPON 100XOTIRF/1.49 oil objective lens. For live cell
296 imaging, a cellVivo incubation module was used to maintain cells at 37°C and 5% CO_2. For analysis of
297 mitochondrial branch length and footprint, the MiNA plugin (36) was used on Fiji. Number and size of
298 PLA puncta, mitochondrial nucleoids, lipid droplets and endosomes were performed using the particle
299 analysis tool on Fiji, following thresholding. All co-localization studies were performed using the JaCoP
300 plugin (37) on Fiji. Extra-mitochondrial mtDNA nucleoids were quantified using the mitoQC plugin on FIJI
301 (38), setting the mtDNA as 'red' signals and mitochondria as 'green' signals. Mito-endosome distances
302 were calculated by quantifying average linear distance between respective signals. All quantitative
303 figures and statistical tests were performed using GraphPad Prism 9.

304

305 **Results**

306 **Patient Report, Whole Exome Sequencing and Protein Expression for MFN2 Q367H Variant**

307 A male patient in their 70s years presented with a two-year history of slowly progressive
308 weakness affecting his lower extremities. Initial symptoms included difficulty walking uphill, and he
309 eventually developed difficulty with stairs and limitations with walking on the ground level and rising
310 from a chair. There were no cramps, fasciculations, or contractures. No sensory loss or coordination.
311 Dysarthria, dysphagia, ptosis, or diplopia were not present.

312 The patient was medically well and did not have any history of cardiac disease. The parent of the
313 proband developed weakness in her lower legs in her 60s, with progressive limitations in her mobility.
314 Apparently, she was diagnosed with CMT disease, but her clinical profile was not available for review.
315 The parent died in her early 80s due to congestive heart failure. The parent's two siblings aged 86-80,
316 and her other two children of ages 40-45 were all unaffected. Clinical examination of the patient
317 demonstrated a cognitively normal individual. Cranial nerve examination was normal. Motor
318 examination revealed MRC grade 4+ strength for ankle dorsiflexion and 4+ plantarflexion bilaterally.
319 Proximal and axial muscle testing was normal, except for Achilles tendon reflexes. The sensory
320 examination was normal. Creatine kinase enzyme activity was elevated to a maximum of 455 U/L
321 (reference range ≤ 195 U/L). The muscle biopsy showed necrotic and regenerating myofibers, myofiber
322 hypertrophy, excessive endomysial and perimysial fibrosis, and extensive infiltration by adipose tissue.
323 Immunostaining for dystrophin, alpha/gamma sarcoglycan, spectrum, α-laminin, desmin, and α-β-
324 crystallin was unremarkable (Figure 1A). There was no inflammatory cell infiltrate. For the magnetic
325 resonance imaging (MRI) examination, upper and lower legs revealed fatty infiltration of the adductor
326 longus gluteus minimus, tibialis anterior, and inferior gastro-soleus bilaterally (Figure 1G/H).

327 The case was interpreted as a chronic myopathy with nonspecific muscle pathology. A genetic
328 cause was suspected given the family history of a similar condition in his parent, and lack of
329 inflammation on muscle biopsy. Clinical testing with a gene panel encompassing 200 genes associated
330 with myopathy, neuropathy, and neuromuscular disorders identified a previously uncharacterized
331 heterozygous variant in the *MFN2* gene, c.1101G>C, p. (Gln367His) [Table 1/Figure 2A]. Research based
332 exome sequencing again identified the MFN2 variant, as well as heterozygous variants of unknown
333 significance in *SYNE1* and *DYSF* (Table 1). While pathogenic variants in *SYNE1* can be associated with
334 autosomal dominant neuromuscular disease, this patient variant was not considered to be clinically
335 relevant for the following reasons: (a) the variant is not in the same domain as pathogenic variants
336 previously associated with autosomal dominant disease, (b) *SYNE1* variants in this region of the gene

337 have only been associated with autosomal recessive disorders, while our patient is heterozygous, (c) no
338 characteristic nuclear abnormalities associated with pathogenic variants in *SYNE1* (39) were observed in
339 patient fibroblasts under microscopy, (d) the myopathy phenotype is not in keeping with the *SYNE1*-
340 related disease phenotype, which includes proximal weakness and contractures. Meanwhile, the *DYSF*
341 variant was not considered to be an explanation for this patient's disease because it is a single
342 heterozygous variant in a condition caused by biallelic variants in DYSF, and we are not aware of any
343 reports of dysferlinopathy associated with only a single pathogenic variant. Thus, based on strong
344 suspicion for the relationship between the MFN2 variant and the patient phenotype, we proceeded with
345 the studies described in this report using patient fibroblast cells.
346
347 **Characterization of Patient Fibroblasts:**
348 To investigate if the Q367H variant contributes to the patient phenotype, we began by examining
349 skin fibroblasts obtained from the patient. Immunoblotting for mitochondrial fusion proteins revealed no
350 significant changes in the expression of MFN2, MFN1, or the inner mitochondrial membrane fusion
351 protein OPA1 (Figure 2C-G). Next, to determine if this MFN2 variant may contribute to the pathology and
352 to gain potential insight into the disease mechanism(s), we characterized patient fibroblasts for
353 alterations to a variety of MFN2-mediated functions.
354
355 **Mitochondrial Network Morphology and Respiration in MFN2 Q367H Fibroblasts**
356 First, as fibroblast cells from CMT2A patients with MFN2 variants sometimes have fragmented
357 mitochondria (17), we examined mitochondrial morphology as a potential downstream readout of
358 altered mitochondrial fusion (Figure 3A-C). No changes were observed under standard culture
359 conditions. However, glucose-free growth conditions supplemented with galactose, which forces cells to
360 use mitochondria for energy rather than glycolysis, can be used detect morphology changes in
361 fibroblasts from patients with MFN2 variants (40). Consistent with decreased mitochondrial fusion and
362 mitochondrial dysfunction, Q367H patient fibroblasts grown in glucose-free galactose-supplemented
363 media showed a marked increase in the number of cells with fragmented mitochondrial networks, as
364 well as a decrease in average mitochondrial length. Impairment of mitochondrial function in patient
365 fibroblasts was further reinforced by functional studies of oxygen consumption. Patient fibroblasts had
366 increased basal oxygen consumption but reduced maximal oxygen consumption (Figure 3D). We also
367 measured mitochondrial membrane potential using TMRE, but did not observe and significant
368 differences in between control and patient cells (Figure 3E). As mitochondrial fragmentation alone does

369 not indicate MFN2 dysfunction (*e.g.*, reduced mitochondrial health in general can lead to mitochondrial
370 fragmentation), we also explored other functions performed by MFN2 to provide additional evidence for
371 MFN2 dysfunction.
372
373 **Perturbated Mitochondrial Nucleoids in MFN2 Q367H Patient Fibroblasts**
374 Mitochondria house their own genome, mtDNA, which is present in hundreds of copies
375 throughout the mitochondrial network and is organized into nucleoid structures. As mtDNA nucleoids
376 can be altered by impairments to mitochondrial fusion (41), we sought to examine mtDNA in Q367H
377 patient fibroblasts (Figure 4A/B). Similar to mitochondrial morphology, there were no changes to mtDNA
378 nucleoid size or abundance in standard media. However, under glucose-free galactose-supplemented
379 conditions, patient fibroblasts had a decrease in the average number of mitochondrial nucleoids per cell,
380 while the average nucleoid size was increased (Figure 4A/C). Of note, in both growth conditions, a small
381 number of mtDNA nucleoids were observed outside the mitochondrial network in patient fibroblasts
382 (circled in Figure 4A). Meanwhile, the mtDNA copy number did not change under any conditions (Figure
383 4D/E), nor were any mtDNA deletions detected (Figure 4F). Observing fewer, larger nucleoids without
384 changes in mtDNA copy number is likely due to nucleoid clustering, a phenotype often observed with
385 impaired mitochondrial fusion (41). As such, the mtDNA studies are consistent with reduced fusion
386 leading to mitochondrial fragmentation in the Q367H cells when grown in glucose-free galactose-
387 supplemented media.
388
389 **MFN2 Q367H Fibroblasts show reduced number of Mito-ER Contact Sites**
390 MFN2 also mediates mito-ER contact sites (MERCs) (42). As an estimate of MERCs, we used a
391 proximity ligation assay to detect regions where the mitochondria and ER are within ~40 nm. Co-
392 localization analysis of the PLA signal with either mitochondrial or ER (Supplemental Figure 1) was used
393 to validate the PLA signal as representative of MERCs. No absolute changes in the number or size of the
394 PLA signals were observed in standard media. However, under glucose-free conditions, Q367H cells had
395 fewer PLA puncta, though these puncta were slightly larger (Figure 5A-C). As changes in MERCs could be
396 due to global changes in mitochondrial abundance, we also measured the area of mitochondria
397 (mitochondrial footprint). Importantly, we do not observe significant differences between mitochondrial
398 footprint in control and patient cells (Figure 5D). However, when the MERC PLA signal is normalized to
399 the mitochondrial footprint, we see a slight a reduction in the number of MERCs in the patient
400 fibroblasts in standard conditions, which is further exaggerated under glucose-free conditions (Figure

401 5E). Together, these data indicate perturbations in MERCs in the Q367H fibroblasts that are consistent
402 with MFN2 dysfunction.
403
404 **Dysfunction in Mitochondrial Fatty Acid Import Leads to Lipid Droplet Accumulation in Patient**
405 **Fibroblasts**
406 Given the role of MFN2 in mediating mitochondria-lipid droplet interactions, and the fact that
407 lipid droplets are altered in fibroblasts from patients with MFN2 variants (17), we next explored lipid
408 droplets in the Q367H fibroblasts. Interestingly, we see a significant increase in the number and size of
409 cellular lipid droplets in patient fibroblasts, both grown in standard and glucose-free galactose-
410 supplemented media (Figure 6A-D). To explore the mechanism underlying the increased accumulation of
411 lipid droplets, we examined lipid transfer from lipid droplets to mitochondria using an assay that takes
412 advantage of the BODIPY 558/568 fatty acid precursor (43). In this assay, the fluorescently labelled lipid
413 is loaded into lipid droplets during a 24-hour incubation, and its transfer to mitochondria can be
414 monitored over time by microscopy. In control cells in standard conditions, some fatty acid pre-cursor
415 transfers into the mitochondrial network (Figure 6E-F), with higher transfer under glucose starvation
416 conditions (without galactose supplementation). Notably, in patient fibroblasts, no fatty acid trafficking
417 from lipid droplets to mitochondria is observed under either growth condition (Figure 6E-F). These
418 findings suggest that the excess lipid droplets seen in the patient fibroblasts are due to an accumulation
419 of lipids due to a lack of fatty acids transfer from lipid droplets to mitochondria.
420
421 **MFN2 Q367H Patient Cells Show mtDNA-Mediated Inflammation**
422 Following up on observation of nucleoids outside of the mitochondrial network (Figure 4), we
423 looked for evidence of mtDNA-mediated inflammation, which is linked to impaired mitochondrial fusion
424 and can cause myopathy (4). First, to look for signs for an inflammatory response, we examined the
425 expression of several inflammation genes via q-RT-PCR. Notably, even when cells were grown in standard
426 glucose conditions, we observed an elevation of genes that mediate TLR9 signalling (*i.e.*,
427 ASC/NLRP3/S100A9) and downstream cytokines of the TLR9 pathway (*i.e.*, IL6/TNFα), as well as genes
428 downstream of the cGAS-STING pathway (INF-α/β) (Figure 7A). Similar inflammatory signalling was
429 observed when fibroblasts were grown in galactose media (Supplemental Figure 2). To determine if the
430 increased expression of these genes was due to the TLR9 or cGAS-STING signalling pathways, fibroblasts
431 in standard media were treated with chloroquine to inhibit TLR9 signalling (44), or RU.521 (45) to inhibit
432 cGAS (Figure 7A). Strikingly, chloroquine reduced TLR9 targets, while RU.521 reduced cGAS-STING

433 targets. The fact that each treatment significantly reduced expression of the relevant genes to the levels
434 seen in the control patient fibroblasts, confirms that both TLR9-NF-kB and cGAS-STING signalling are
435 elevated in the patient fibroblasts and that these are the primary pathways driving inflammation.
436 Given the link to TLR9 signalling, which detects mtDNA in endosomes, we also looked to see if
437 mtDNA outside the mitochondrial network colocalized with Rab5C-labelled early endosomes.
438 Remarkably, we observed co-localization of extra-mitochondrial mtDNA with early endosomes, including
439 enlarged endosomes harbouring several mtDNA nucleoids (Figure 7B-C). Overall, these findings point to
440 a mtDNA-mediated sterile inflammatory response, mediated through localization of mtDNA into early
441 endosomes and the cytosol (Figure 7D).
442
443 **MFN2 Q367H Patient Transdifferentiated Myoblasts Show Elevated Inflammation, Disrupted MERCs**
444 **and Reduced mtDNA Nucleoid Content**
445 To examine the cellular and inflammatory phenotypes more closely in a relevant cell type, we
446 transdifferentiated control and patient fibroblasts into myoblasts for additional characterization. Upon
447 transdifferentiating, we still observed increased inflammatory signalling (Figure 8A). However, compared
448 to fibroblast cells, patient myoblasts exhibited an additional 3-fold increase in cGAS-STING interferons,
449 and a 10-fold increase in the TLR9 inflammatory signalling, indicating that these pathways are even more
450 strongly activated in patient muscle cells. Finally, we examined some basic parameters of MFN2
451 functions in our transdifferentiated patient myoblasts. First, we found no changes in gross mitochondrial
452 morphology or the average length of mitochondrial branches in patient myoblasts (Figure 7B-C). Second,
453 patient myoblasts had fewer MERCs, which were also smaller in size (Figure 8D-F). Finally, the mtDNA
454 nucleoid analysis found a reduction in the number nucleoids per cell in patient myoblasts, as well as a
455 decrease in size of the nucleoids (Figure 8G-I). Notably, consistent with findings in patient fibroblasts, a
456 subset of these nucleoids could be found outside of the mitochondrial network.
457
458 **Re-Expression of MFN2 Q367H in MFN2 KO Cells Recapitulates mtDNA Release Phenotype**
459 To determine if the MFN2 Q367H variant is sufficient to induce the mitochondrial alterations
460 that we observed in patient fibroblasts, we re-expressed either WT MFN2 or the Q367H variant in U2OS
461 MFN2 KO cells (Figure 9)(Supplemental Figure 3). As MFN2 overexpression can induce artefacts (46), we
462 first confirmed that MFN2 was expressed at endogenous levels (Figure 8B). Validating our KO re-
463 expression approach, we found that WT MFN2 re-expression restored all the phenotypes we observed in
464 the U2OS KO cells (Figure 9) (Supplemental Figure 3). In line with the normal mitochondrial morphology

465 observed in patient fibroblasts grown in glucose and myoblasts, the mitochondrial network in the Q367H
466 re-expression cells was also restored (Figure 9A,C), further suggesting this variant is competent for
467 mitochondrial fusion. With respect to the number and size of mtDNA nucleoids, the Q367H re-
468 expression cells fell between the extremes in the WT and MFN2 KO cells (Supplemental Figure 3A,B).
469 Next, we focused on the unique mtDNA release phenotype seen in the Q367H patient cells. Despite the
470 ability of the Q367H variant to restore mitochondrial morphology, and consistent with our earlier
471 observations in patient cells harboring the Q367H variant, there was a prominent presence of mtDNA
472 outside the mitochondrial network in the U2OS MFN2 KO cells re-expressing Q367H (Figure 9A)
473 (Supplemental Figure 3C), and this mtDNA was predominantly co-localized with endosomes (Figure 9C)
474 (Supplemental Figure 3D,E). Intriguingly, there were significant differences between MFN2 KO and the
475 Q367H re-expression lines with respect to mtDNA release. For example, while there was slightly more
476 extra mitochondrial mtDNA in U2OS KO cells, only about half of the mtDNA co-localized with endosomes
477 in the MFN2 KO cells (Supplemental Figure 3C-E). Moreover, compared to MFN2 KO cells, endosomes in
478 the Q367H re-expression cells were more abundant, larger, and on average closer to mitochondria
479 (Supplemental Figure 9F-H). Overall, these findings show that while the Q367H variant is competent for
480 mitochondrial fusion, it is sufficient to cause mtDNA release, and that mtDNA/endosome colocalization
481 and endosome phenotypes are exacerbated with the Q367H variant compared to the MFN2 KO cells.

482 **Discussion:**

483 We report an individual with a late-onset myopathy phenotype and a previously uncharacterized
484 variant in *MFN2*. We pursued the investigations described in this report based on strong clinical
485 suspicion for this as a potential pathogenic variant. This sequence change in *MFN2* replaces glutamine
486 with histidine at codon 367 of the MFN2 protein (Q367H). The glutamine residue is highly conserved,
487 and there is a small physicochemical difference between glutamine and histidine, implying a
488 hypermorphic change. The MFN2 Q367 amino acid is conserved across vertebrate MFN2 sequences, as
489 well as with the MFN1 paralogue (Figure 2B). The MFN2 Q367H variant is present in population
490 databases with a very low allele frequency (highest allele frequency 0.000242 in Gnomad according to
491 dbSNP report rs373211062, accessed June 4, 2024), including one homozygous individual. The variant
492 has an entry in Clinvar (439898, accessed June 4, 2024) and is classified as having conflicting
493 interpretations of pathogenicity, with 4 entries from clinical testing of patients with neurological
494 phenotypes. In a large cohort study, a patient with early onset peripheral neuropathy was reported who
495 was compound heterozygous for Q367H and P184R MFN2 variants (47). However, the
496 Q367H MFN2 variant has not been functionally characterized, or previously reported in the literature as
497 a standalone disease-causing variant. The family history of the patient's parent suggests autosomal
498 dominant inheritance, which is in keeping with this variant, although confirmation of this variant was not
499 possible in the parent. Furthermore, a different amino acid substitution at this position (Q367P) was
500 associated with a neuropathy presentation (48), providing additional support that variants at this
501 position are likely to be associated with this disease. All considered, the Q367H variant is highly plausible
502 as a reduced penetrance pathogenic variant given its extremely low frequency in population databases,
503 its prevalence in individuals with neurological phenotypes, its presence in published cases from
504 literature. The data from studies in this report point to the deleterious nature of the Q367H variant, and
505 importantly demonstrate the damaging effect of this variant in cells transdifferentiated to the muscle
506 lineage.

507 This case illustrates many of the challenges when conducting research with people affected by
508 genetic conditions with very late onset. Information from control population databases may be
509 misleading if individuals are presymptomatic for a very late onset disease, or when phenotypes are very
510 mild and slowly progressive. Even for paediatric-onset disease, pathogenic variants appear in a
511 substantial proportion of control individuals (2.8% in one study) (49) , and this number may be
512 comparable or even higher for very-late onset disorders, such as the one described in this report. Future
513 research will improve our understanding of genetic variants and disorders with very late onset and

514 variable penetrance, but identification and investigation of cases is difficult since they may be mistaken
515 for degenerative or acquired conditions (for example, prior work showing diagnoses of genetic spastic
516 paraplegia in patients initially diagnosed with sporadic primary lateral sclerosis)(50). Other factors
517 include the lack of availability of family members for segregation of variants (i.e: parents have expired by
518 the time the patient is diagnosed, or family members are estranged, or the disease status is not yet
519 known for younger family members). In this respect, we acknowledge the limitations of this study, which
520 only includes a single affected participant. However, we hope to bring attention to the fact that the
521 investigation of genetic disorders is important to our broader understanding of genetic diseases and
522 operates with the above-mentioned special challenges. Furthermore, our findings from the re-
523 expression of the variant in a KO cell line show the importance of functional characterization to confirm
524 potential pathogenic variants.

525 Despite the fact that over 150 MFN2 variants have been reported in patients with CMT2A, we
526 still do not have a complete understanding of how MFN2 dysfunction contributes to disease. The
527 situation is complex, as MFN2 has multiple functions in the cell, and CMT2A can have additional
528 pathological phenotypes beyond peripheral neuropathy. Moreover, only a handful of MFN2 variants have
529 been characterized functionally, and even then, often only for one or two of MFN2's known functions
530 (17). Thus, a better understanding of how MFN2 variants affect MFN2 functions is essential to
531 understanding how MFN2 contributes to disease. Here, our characterization of cells from a patient
532 exhibiting distal myopathy who carried the candidate pathogenic MFN2 Q367H variant provides novel
533 mechanistic insight into MFN2-mediated pathology. The fact that several MFN2-mediated functions are
534 impaired in the patient cells, especially when they are forced to use mitochondria for energy production,
535 supports the notion that the Q367H variant impairs MFN2 function and likely contributes to the patient
536 pathology. Moreover, to our knowledge, the association of mtDNA release and inflammation with an
537 MFN2 variant has not been reported previously, and supports a mechanistic pathway by which MFN2
538 dysfunction contributes to inflammation. Finally, the elevated levels of inflammation in patient-derived
539 transdifferentiated myoblasts further support a novel disease pathomechanism for MFN2-mediated
540 inflammation driving myopathy.

541 Several lines of evidence support the pathogenicity of the Q367H MFN2 variant. Patient
542 fibroblasts show perturbation to multiple functions performed by MFN2, including mitochondrial fusion
543 mtDNA nucleoid distribution, MERCs and cellular lipid droplets. Similarly, characterization of our Q367H
544 re-expression line also provides direct evidence that this variant is not fully functional. With respect to
545 mitochondrial fusion, similar to our findings, several MFN2 variants do not show mitochondrial

546 fragmentation when grown in standard glucose conditions (17). However, culturing fibroblasts in
547 galactose can reveal fragmentation of the mitochondrial network, as reported for MFN2 D210V (10), and
548 as we see for the Q367H variant. This network fragmentation could be caused by reduced fusion and/or
549 increased fission, which can occur in response to a variety of stimuli (51). Given the well-defined role of
550 MFN2 in mitochondrial fusion, the fragmentation is consistent with reduced fusion. Meanwhile, as
551 reduced mitochondrial fusion can also impact mtDNA distribution (41), the changes we see in
552 mitochondrial nucleoids are also consistent with reduced fusion in patient fibroblasts when grown in
553 galactose. Nevertheless, the Q367H re-expression line shows that this variant can restore mitochondrial
554 morphology in MFN2 KO cells. Thus, any impairment in mitochondrial fusion is likely to be minor, and
555 only noticeable under conditions such as when grown in galactose.

556 Beyond mitochondrial fusion, perhaps the best characterized function of MFN2 is in regulating
557 MERCs (2). Notably, MERCs in fibroblasts from patients with various *MFN2* variants can show a variety of
558 changes (17), and the reduction in the number and size of MERCs that we observed in patient cells is
559 consistent with MFN2 dysfunction. Intriguingly, altered MERCs could contribute to the patient myopathy,
560 as pathogenic variants in *SEPN1*, another gene implicated in MERC biology, also causes a myopathy
561 phenotype (52).

562 Also consistent with MFN2 dysfunction and in line with our findings, an increased number and
563 size of lipid droplets in fibroblasts is reported in fibroblasts patients with other MFN2 variants (53), as
564 well as upon MFN2 depletion (3). Intriguingly, the lipid droplet phenotype is evident in standard growth
565 conditions when mitochondrial morphology was unaltered. Notably, the mechanism by which impaired
566 MFN2 function leads to increased size and abundance of lipid droplets in patient fibroblasts has not
567 been investigated previously. We envision several possible explanations: decreased transfer of lipids into
568 mitochondria from lipid droplets, or increased transfer of lipids from mitochondria to lipid droplets. Our
569 finding that patient fibroblasts failed to import fatty acids into mitochondria, even under glucose
570 starvation conditions, is in line with the first possibility, and likely reflects the role of MFN2 in mediating
571 mitochondria-lipid droplet interactions (54). Though we expect reduced lipid transfer will also explain
572 the increased lipid droplet accumulation observed in fibroblasts from patients with other MFN2 variants,
573 this remains to be determined.

574 Characterization of the transdifferentiated patient myoblasts provides further evidence of MFN2
575 dysfunction and important insight into the muscle myopathy phenotype in the patient. Consistent with
576 MFN2 dysfunction, we see a significant decrease in the number and size of mitochondrial nucleoids, as
577 well as fewer and smaller MERCs in transdifferentiated patient myoblasts. However, we did not observe

578 any changes in mitochondrial network morphology. Notably, the transdifferentiated myoblasts were
579 grown in standard myoblast media, as opposed to the glucose-free galactose-supplemented media
580 required to elicit differences in the patient fibroblasts. Other differences in growth conditions between
581 transdifferentiated patient myoblasts (*e.g.*, collagen matrix), or the inherent differences between
582 fibroblast and myoblast cell types may also explain differences between patient fibroblasts and
583 transdifferentiated myoblasts. Regardless, the reduced number of nucleoids in the patient cells is
584 consistent with MFN2 dysfunction, as muscle-specific loss of MFN2 leads to mtDNA depletion (18).
585 The finding of mtDNA release and inflammation in both Q367H patient fibroblasts and
586 transdifferentiated myoblasts is novel in the context of pathogenic MFN2 variants and is likely relevant to
587 disease mechanism. The mtDNA release and endosome co-localization also observed in the Q367H re-
588 expression cells further shows that this variant causes mtDNA release, rather than an undetected
589 difference in the genetic background of the patient. With respect to the inflammatory signals, the fact
590 that inhibitors of both TLR9/cGAS-STING pathways lead to decrease in their downstream cytokines,
591 indicates that both pathways are activated. These findings are also consistent with previous work on
592 impaired mitochondrial fusion and increased inflammation. With respect to MFNs, a recent paper by
593 Irazoki *et al.*, found that knockdown of either MFN1 or MFN2 in myoblasts could promote TLR9 signalling
594 (4). Arguing that activation of TLR9-mediated inflammation is a general response to loss of mitochondrial
595 fusion, loss of the inner mitochondrial membrane fusion protein OPA1 in muscle leads to TLR9-mediated
596 NF-κB activation (but not cGAS-STING), where it also drives an inflammatory myopathy (55). Thus, it
597 seems that loss of fusion is sufficient to induce mtDNA-mediated TLR9 inflammation in muscle cells that
598 can drive myopathy. A mechanism that may explain the phenotype of the patient harbouring the Q367H
599 variant. Meanwhile, the increased cGAS-STING signalling that we also see in Q367H patient cells is
600 consistent with increased cGAS-STING activity also reported in MFN2-deficient myoblasts (4), as well as
601 in microglia where MFN2 is downregulated (56). Whether cGAS-STING signalling further perturbs
602 pathology remains to be determined, though elevated cGAS-STING inflammation is also linked to
603 myopathy (57).
604 Another interesting question involves how MFN2 loss of function drives mtDNA release to
605 stimulate both TLR9 and cGAS-STING inflammation. In this regard, several recent studies are relevant to
606 endosomal-mediated mtDNA release (58–60). A model seems to be emerging where, in the context of
607 stalled mtDNA replication intermediates, enlarged nucleoid clusters are transferred directly into early
608 endosomes, where the mtDNA can be detected by TLR9. When this quality control pathway is
609 overwhelmed, it can lead to release of mtDNA from endosomes into the cytosol, and cGAS-STING

610 activation (60). Notably, one mechanism by which loss of mitochondrial fusion is proposed to impact the
611 mtDNA is through imbalanced distribution of mtDNA maintenance proteins (61), which may lead to an
612 increased abundance of stalled mtDNA replication intermediates. Thus, mtDNA replication fork stalling in
613 response to impaired mitochondrial fusion may trigger initial mtDNA release into endosomes, and the
614 subsequent TLR9 activation associated with MFN2 dysfunction. The fact that we see extra mtDNA and
615 inflammatory signalling in patient cells with normal mitochondrial morphology (*e.g.*, fibroblasts grown in
616 standard media, and differentiated myoblasts), suggests that even subtle alterations in mitochondrial
617 fusion are sufficient to impact the mtDNA. Alternatively (or in conjunction), the differences in MERCs,
618 which can demarcate sites of mtDNA replication (62,63), could also impair mtDNA replication and trigger
619 to mtDNA release into endosomes.

620 Meanwhile, as elevated cGAS-STING is not found with MFN1 or OPA1 depletion (4,55,64), the
621 elevated cGAS-STING signalling in myoblasts devoid of MFN2 (4), and seen here in MFN2 Q367H patient
622 cells, suggests another role for MFN2 in mediating mtDNA release beyond just reduced mitochondrial
623 fusion. In this regard, MFN2 can interact with RAB5C on early endosomes (4). As such, it is tempting to
624 speculate that MFN2 has a role in mediating the mitochondrial-endosome interactions required for
625 endosome-mediated removal of stalled mtDNA replication intermediates, and that altering this
626 interaction promotes mtDNA escape into the cytosol to activate cGAS-STING inflammation. In this
627 regard, the differences between MFN2 KO and Q367H re-expression cells with respect to endosomal
628 mtDNA and endosome alterations support the notion that the Q367H variant is not just 'loss of function'
629 with respect to mtDNA release. Future studies examining the mechanisms of mtDNA release will likely
630 provide more insight to the role played by MFN2 and may benefit from examining the Q367H variant as a
631 means to perturb MFN2 function.

632 It is worth noting that MFN2 could also influence inflammation through its other functions. For
633 example, there are connections between disrupted MERCs and activation of sterile inflammation,
634 particularly in high energy-demanding tissues such as the heart (65). Meanwhile, relevant to the
635 increased lipid droplet abundance associated with MFN2 dysfunction and seen even in standard growth
636 conditions with normal mitochondrial morphology, it is notable that lipid droplet biology intersects with
637 inflammation. Specifically, elevated lipid droplet abundance correlates with increased inflammation (66–
638 69). Overall, our findings are consistent with MFN2 dysfunction contributing to inflammation, which is a
639 possible explanation for myopathy initially described in the proband.

640 The patient presentation, with late onset myopathy, but without neuropathy, offers a unique
641 opportunity to separate the pathological outcomes of MFN2 dysfunction by examining the specific

642 mechanism leading to myopathy. Although myopathy has been reported previously in patients with
643 CMT2A (11,12), it has always been in the context of a peripheral neuropathy where it is generally
644 considered to be a downstream consequence of nerve loss. For example, the MFN2 D210V variant has
645 myopathy phenotypes in a three-generational case study, which has accompanying axonal neuropathy
646 (10). On the other hand, arguing against the notion of muscle loss downstream of neuropathy,
647 mitochondrial myopathy is seen in a skeletal muscle-specific MFN2 loss-of-function study in animal
648 models, highlighting the importance of the protein in tissues such as skeletal muscle (70,71). Meanwhile,
649 in cardiac muscle, the MFN2 R400Q variant is implicated in cardiomyopathy, though no link to
650 inflammation was investigated (72). Additionally, the loss of MFN2 protein expression in skeletal muscles
651 correlates with age and could contribute to sarcopenia through a similar inflammatory mechanism (73).
652 Finally, similar to the patient we describe here, a novel ENU-induced Mfn2 mouse model characterized
653 L643P as a variant that causes muscle myopathy without peripheral neuropathy (74). Together, these
654 findings show that MFN2 dysfunction can cause muscle myopathy in the absence of nerve degeneration,
655 as observed in the proband. Future cases of myopathy associated with this variant in MFN2 may benefit
656 from the inclusion of electron microscopic examination of muscle biopsy tissues. EM was not obtained
657 for our case, but may have shown mitochondrial ultrastructural changes to provide further insight into
658 the morphological impacts of the MFN2 variant.
659 With respect to how MFN2 dysfunction might cause myopathy, in the first report of an MFN2-
660 specific mouse muscle knockout, the authors argued that the mtDNA depletion was likely a key
661 contributory factor due to reduced oxidative phosphorylation (70). However, more recent work linking
662 MFN1 and OPA1 muscle deficiency to inflammation mediated myopathy, showed that blocking the
663 inflammation was protective in these models (4,55), arguing for a key role of inflammation in the muscle
664 pathology caused by impaired mitochondrial fusion. Mechanistically, inflammation in the muscle cell
665 niche can lead to myopathy and interfere with muscle stem cell populations (75), as well as affect the
666 expression of myogenic genes (76). Meanwhile, NF-kB, a proinflammatory cytokine that is downstream
667 of TLR9 signaling, can cause muscle wasting in mice (77). Building on these findings, it is tempting to
668 speculate that mtDNA-mediated inflammation may also be relevant to idiopathic inflammatory
669 myopathies, a heterogeneous group of autoimmune disorders with varying clinical manifestations,
670 primarily defined by muscle weakness (78,79). In this regard, we speculate that the mtDNA-mediated
671 inflammation discovered in Q367H patient-derived cells is contributing to the patient myopathy.
672 Although MFN1 and OPA1 deficiency can cause inflammatory myopathy in mouse muscle
673 knockout models, the role of mtDNA-mediated inflammation in MFN2 pathology has not been fully

674 explored. While a mouse knock-in model of the MFN2 K357T variant is linked to augmented
675 neuroinflammation in response to LPS treatment, the role of mtDNA was not investigated (80). Our
676 findings linking the MFN2 Q367H variant to mtDNA release and inflammation thus provide a novel
677 disease mechanism for MFN2 dysfunction. Moreover, while our findings are relevant to the myopathy
678 phenotype in muscle, it is also possible that mtDNA-mediated inflammation contributes to the
679 peripheral neuropathy in neurons. Intriguingly, peripheral neuropathy is a common phenotype of several
680 DNA damaging agents (81–85) , such as doxorubicin, which can damage mtDNA and lead to mtDNA-
681 mediated cGAS-STING inflammation (86).
682 In summary, we observed elevated mtDNA-mediated TLR9/NF-kB and cGAS-STING inflammatory
683 signaling in a patient harboring the uncharacterized MFN2 Q367H variant who displayed late-onset
684 myopathy as a standalone phenotype. Moreover, functional analyses of patient fibroblasts provided
685 several lines of evidence consistent with MFN2 dysfunction. Critically, characterization of
686 transdifferentiated myoblasts and the elucidation of a novel link to mtDNA-mediated inflammation may
687 mechanistically explain the myopathy phenotype in the patient.
688

689 **Acknowledgements**
690 The authors would like to thank the study participants and their family. Lentivirus production
691 was performed by the Hotchkiss Brain Institute Molecular Core Facility at the University of Calgary.
692

693 **Conflict of Interests**
694 The authors declare that they have no conflict of interest.
695

696 **Author contributions**
697 Designed and/or performed and analyzed mitochondrial experiments, MZ, GS, WA, TS, RS, MJ,
698 AM, CC GP, and TES; Clinical evaluation of patients, GP, JTJ; Analyzed exome data GP, MJ; Performed skin
699 biopsy from mitochondrial patients, GP; Drafted the manuscript or figures, MZ, GP, TES. All authors
700 discussed the results and commented on the manuscript. GS, and WA are joint second authors. TES and
701 GP are co-corresponding authors.
702

703 **Funding**
704 This work was supported by funds provided by the Alberta Children's Hospital Research Institute
705 (TES), the Canadian Institutes of Health Research (TES), and the New Frontiers Research Fund (TES). MZ

706 was supported by a Hotchkiss Brain Institute International Recruitment Scholarship. WA was supported
707 by the Saudi Cultural Bureau. R.S. was supported by a QEII Graduate Scholarship. TGBS was supported by
708 an Alberta Graduate Excellence Scholarship and a University of Calgary Faculty of Graduate Studies
709 Doctoral Scholarship. MJ is the recipient of the Katharine Sarah Melinda Mei-Ling Thomas Rare Diseases
710 Scholarship. Infrastructure in the lab of GP for this work was supported by the HBI Dementia Research
711 Equipment Fund and a Canada Foundation for Innovation JELF Grant (Neuromuscular Genetics, 36624).
712 The funders had no role in study design, data collection and interpretation, or the decision to submit the
713 work for publication.

714 **Figure Legends:**

715

716 **Figure 1: Muscle pathology findings.**

717 Representative images of the muscle biopsy (A-F) including two formalin-fixed, paraffin-embedded slides
718 (panels A and F) and four snap-frozen muscle sections (panels B-E). Distances are represented in the
719 scale bars. Panel A (hematoxylin-eosin; H&E) demonstrates extensive adipose tissue ("fatty
720 replacement") in the biopsy (black arrow). This was less obvious in the frozen tissue, which had been
721 dissected away from obvious fat. Panel B (H&E) illustrates the variation in myofiber size, as well as the
722 increased connective tissue between myofibers (endomysial fibrosis; green arrow). The biopsy had
723 several necrotic fibers (panel C H&E; black arrow) and increased numbers of internalized nuclei (black
724 arrowhead). In panel D (H&E) are two basophilic regenerating fibers (black arrows), internalized nuclei
725 (black arrowheads), and increased endomysial connective tissue (green arrow). Dystrophin
726 immunoperoxidase stains the myofiber sarcolemma (Dys2 illustrated in panel E). Dys1 and Dys3 are
727 similar (data not shown). The desmin immunoperoxidase in longitudinal sections (panel F) illustrates the
728 repetitive sarcolemmal units (stripes in each fiber) but does not stain significant sarcoplasmic deposits.
729 G. MRI image at the level of the legs demonstrating predominant atrophy in white arrows;
730 Gastrocnemius (i), Soleus (ii) and Tibialis Anterior (iii) bilaterally. H. MRI image of upper thighs
731 demonstrating predominant atrophy of adductor longus gluteus minimus.

732

733 **Figure 2: Initial characterization of MFN2 Q367H variant.**

734 A.(i) Sanger sequencing results showing single nucleotide polymorphism in patient fibroblasts, transition
735 Guanine to Cytosine. (ii) Topology diagram of MFN2 protein with domains and localization indicated. The
736 site of the Q367H variant is shown in the diagram. B. Amino acid sequence alignment using T-COFFEE
737 tool. C. Western Blot analysis comparing expression of mitochondrial fusion protein in control vs patient
738 fibroblasts, normalized to β-actin. (D-G) Comparison of protein expression levels (D) MFN2 (glucose
739 media) (E) MFN2 (glucose-free/galactose supplemented media) (F) MFN1 (G) OPA1 levels in control vs
740 patient fibroblasts. Data is indicative of mean +/- SD. Statistical comparisons were made by unpaired t-
741 test, (ns=not significant ($p>0.05$)).

742

743 **Figure 3: Changes in mitochondrial morphology and respiratory function.**

744 (A) Representative confocal images (top) with zoomed inset images (bottom) showing mitochondrial
745 network morphology in control vs patient fibroblasts stained with TOMM20. (B) Qualitative scoring of

746 proportion of cells showing fragmented/intermediate/fused mitochondrial network. Bars indicate mean
747 +/-SD. (C) Quantitative analysis of mean mitochondrial branch length in control vs patient fibroblasts
748 using glucose or glucose-free/galactose supplemented media, bars show mean +/- SD, colours indicate
749 biological replicates. (D) Oxygen Consumption Rate (OCR) assay on control and patient fibroblasts using
750 Seahorse XFe24, bars indicate mean +/- SD (n=12 replicates). Statistical comparisons were made by
751 unpaired t-test. (E) Mitochondrial Membrane potential is reported as mean fluorescent intensity lMFI) of
752 TMRE signal in live cells measured by flow cytometry. Bars indicate mean +/- SEM, points indicate
753 biological replicates, unpaired t-test. (ns=not significant ($p>0.05$); ****=$p\leq 0.0001$).
754
755 **Figure 4: Characterization of mtDNA nucleoids, mtDNA copy number, and mtDNA deletions.**
756 (A) Representative confocal images showing mitochondria (TOMM20; grey) and mitochondrial nucleoids
757 (dsDNA antibody; red) in patient and control fibroblasts under glucose and glucose-free/galactose
758 supplemented nutrient conditions. Circles indicate presence of mtDNA nucleoids outside the
759 mitochondrial network. (B) Number of nucleoids per cell, mean is shown with colours indicating
760 biological replicates. (C) Average size of mitochondrial nucleoids, violin plots show median and
761 interquartile ranges. (D-E) qPCR data showing mitochondrial DNA copy number in (D) glucose and (E)
762 glucose-free/galactose supplemented media, bars indicate mean +/- SD. (F) Agarose gel electrophoresis
763 showing long range PCR products used to detect full-length or deleted mtDNA and DNA ladder showing
764 corresponding sizes. Statistical comparisons were made by unpaired t-test, (ns=not significant ($p>0.05$);
765 *=$p\leq 0.05$; ***=$p\leq 0.001$; ****=$p\leq 0.0001$).
766
767
768 **Figure 5: Mito-ER Contact site alterations.**
769 (A) Representative confocal images of mito-ER contact sites (MERCs) using proximity ligation assay (PLA)
770 showing mitochondria (TOMM20; cyan), PLA probes (green) and ER (Calnexin; magenta) in glucose and
771 glucose-free/galactose supplemented media. (B) Quantitative analysis of number of MERCs per cell, lines
772 indicate mean +/- SD, colours indicate biological replicates. (C) Quantitative analysis of average size of
773 PLA probes, with violin plots indicate median and interquartile range. (D) Quantitative analysis of
774 mitochondrial area in each cell type in (μm^2), lines show mean +/- SD, colours indicate biological
775 replicates. (E) Normalized number of MERCs to total mitochondrial area per cell, lines indicate mean +/-
776 SD, colours indicate biological replicates. P-values determined by unpaired t-test (ns=not significant
777 ($p>0.05$); *=$p\leq 0.05$; **=$p\leq 0.01$; ****=$p\leq 0.0001$).

778

779 **Figure 6: Changes to cellular lipid droplets.**

780 (A-B) Representative confocal images showing lipid droplets stained with HCS LipidTox Green in (A)
781 glucose and (B) glucose-free/galactose supplemented media. (C) Quantitative analysis of the average
782 number of lipid droplets per cell, bars indicate mean +/- SD, colours indicate biological replicates. (D)
783 Quantitative analysis of the average size of lipid droplets, violin plots show median and interquartile
784 range. (E) Representative live-cell confocal images showing mitochondria (MitoTracker Green) and fatty
785 acids (BODIPY 558/568) at 0 hours and 24 hours in standard or glucose-starved media. (F) Quantitative
786 analysis of co-localization between fatty acid and mitochondrial network, colours indicate cell type (red-
787 control and blue-MFN2 Q367H), bars indicate mean +/- SD. P-values determined by unpaired t-test
788 (ns=not significant ($p>0.05$); **=$p\leq 0.01$; ****=$p\leq 0.0001$).

789

790 **Figure 7: MFN2 Q367H cells show activation of TLR9 and cGAS-STING inflammatory pathways, and co-**
791 **localization of mtDNA with early endosomes.**

792 (A) RT-qPCR data showing gene expression for TLR9/NF-KB targets (Asc, IL6, NLRP3, S100a9, TNF) and
793 cGAS-STING targets (Ifn-α, Ifn-β) in control vs patient fibroblasts under glucose conditions. The graph
794 also shows the effects of inhibitors for the TLR pathway (Chloroquine) or cGAS-STING pathway (RU.521).
795 Lines indicate mean +/- SD. (B) Representative confocal images showing mitochondria (TOMM20; cyan),
796 mitochondrial nucleoids (anti-dsDNA antibody; green), and early endosomes (RAB5C; magenta). Images
797 in inset bottom right panel highlights the location of mitochondrial nucleoids outside the mitochondria
798 with the early endosomes, denoted by the white arrows. (C) Quantitative analysis of signal co-
799 localization between mitochondrial nucleoids and early endosomes in patient and control fibroblasts
800 determined by Pearson's coefficient, lines indicate mean +/- SD, points indicate replicates. (D) Pathway
801 model representing mitochondrial dysfunction leading to sterile inflammation. The diagram shows how
802 the MFN2 Q367H variant can alter mitochondrial function, leading to transfer of mtDNA from the
803 mitochondria to the early endosomes (middle). This can lead to detection by TLR9 and subsequent
804 activation of the NF-kB mediated inflammation (right). Additionally, mtDNA in the early endosomes
805 could leak into the cytosol, leading to detection through the cGAS-STING pathway (middle-bottom),
806 promoting Type-I Interferon mediated inflammation (right). Collectively, the inflammation contributes to
807 the distal myopathy disease outcome in the patient. P-values determined by unpaired t-test (ns=not
808 significant ($p>0.05$); *=$p\leq 0.05$; ****=$p\leq 0.0001$).

809

810 **Figure 8: Altered MFN2 functions in transdifferentiated patient myoblasts.**
811 (A) RT-qPCR data showing gene expression for TLR9/NF-KB targets (Asc, IL6, NLRP3, S100a9, TNF) and
812 cGAS-STING targets (Ifn-α, Ifn-β) in control vs patient myoblasts, lines indicate mean +/- SD.(B)
813 Representative confocal images showing mitochondrial network morphology (TOMM20; cyan) in control
814 and patient myoblasts. (C) Quantitative analysis of mean mitochondrial branch length in control and
815 patient myoblasts, violin plots show median and interquartile ranges. (D) Representative confocal images
816 of control and patient myoblasts showing PLA probes (representing MERCs; green), mitochondria
817 (TOMM20; cyan) and ER (Calnexin; magenta). (E) Quantitative analysis of the number of MERCs per cell
818 in control and patient myoblasts, violin plots show media and interquartile ranges. (F) Quantitative
819 analysis of average size of MERCs per cell in control and patient myoblasts, violin plots show media and
820 interquartile ranges. (G) Representative confocal images showing mitochondria (TOMM20) and
821 mitochondrial nucleoids (dsDNA antibody). Circles indicate mtDNA staining outside the mitochondrial
822 network. (H) Quantification of average number of nucleoids per cell in control and patient myoblasts,
823 violin plots show median and interquartile ranges. (I) Quantification of average size of mtDNA nucleoids
824 in control and patient myoblasts. Violin plots show median and interquartile ranges. P-values
825 determined by unpaired t-test (ns=not significant ($p>0.05$); ***=$p\leq 0.001$; ****=$p\leq 0.0001$).
826
827 **Figure 9: Re-Expression of WT MFN2 and MFN2 Q367H in knockout cells.**
828 (A) Representative confocal images showing mitochondria (TOMM20-grey), mtDNA (dsDNA-green) and
829 early endosomes (Rab5-magenta) in U2OS WT, U2OS MFN2 KO, U2OS MFN2 KO cells with re-expression
830 of WT MFN2 and U2OS MFN2 KO cells with re-expression of Q367H MFN2 (left to right). Insets are of the
831 boxed regions in above pictures, dotted circles show mtDNA outside the mitochondrial network, while
832 arrows show mtDNA outside the mitochondrial network and co-localized with early endosomes. (B)
833 Western Blot analyses confirming re-expression of WT MFN2 and MFN2 Q367H in U2OS MFN2 KO cells.
834 (C) Quantitative analyses of mitochondrial network morphology in the four cell lines. (D) Quantitative
835 analyses of Pearson's Co-localization co-efficient between mtDNA and early endosomes in the four cell
836 lines. Colors indicate biological replicates; violins show median and interquartile range. Stats- two-way
837 ANOVA (ns=not significant ($p>0.05$); *=$p\leq 0.05$; **=$p\leq 0.01$; ****=$p\leq 0.0001$).
838

839 **Supplemental Figure 1: Proximity Ligation Assay (PLA) validation.**

840 (A) Pearson's co-localization analysis comparing overlap between PLA signals with mitochondria
841 (TOMM20) or ER (calnexin) in control and patient cells under glucose media. Violin plots indicate median
842 and interquartile range. Statistical analysis was performed via unpaired t-test.

843

844 **Supplemental Figure 2: Inflammatory response in glucose-free media.**

845 (A) RT-qPCR data showing gene expression for TLR9/NF-KB targets (Asc, IL6, NLRP3, S100a9, TNF) and
846 cGAS-STING pathway targets (INFα, INFβ) in control (CF) vs patient fibroblasts (Q367H) under glucose-
847 free media conditions. Colors indicate biological replicates. Error bars indicate mean +/- SD. Statistical
848 analysis was performed via unpaired t-test with the relevant control.

849

850 **Supplemental Figure 3: Re-Expression of WT MFN2 and MFN2 Q367H in knockout cells.**

851 Quantification of additional cellular phenotypes for the indicated cell lines from Figure 8. (A-D)
852 Characterization of mitochondrial DNA (mtDNA) including: (A) nucleoid copy number; (B) nucleoid size;
853 (C)average number of extra-mitochondrial nucleoids; (D) average number of extra-mitochondrial
854 nucleoids within Rab5-positive early endosomes (D); and (E) percentage of extra-mitochondrial
855 nucleoids within Rab5-positive endosomes (F-H) Quantification of Rab5-positive endosomes, including:
856 (F) average number of endosomes; (G) average endosome size; and (H) average distance between
857 mitochondria and endosomes. Colors indicate biological replicates, violin plots show median and
858 interquartile range, while error bars show mean +/- SD. P-values are all determined by two-way ANOVA,
859 (ns=not significant ($p>0.05$); *=$p\leq 0.05$; **=$p\leq 0.01$; ****=$p\leq 0.0001$).

860 **References**

861 1. Filadi R, Pendin D, Pizzo P. Mitofusin 2: from functions to disease. Cell Death Dis. 2018 Feb
862 28;9(3):330.

863 2. de Brito OM, Scorrano L. Mitofusin 2 tethers endoplasmic reticulum to mitochondria. Nature.
864 2008 Dec 4;456(7222):605–10.

865 3. Boutant M, Kulkarni SS, Joffraud M, Ratajczak J, Valera-Alberni M, Combe R, et al. Mfn2 is critical
866 for brown adipose tissue thermogenic function. EMBO J. 2017 Jun 1;36(11):1543–58.

867 4. Irazoki A, Gordaliza-Alaguero I, Frank E, Giakoumakis NN, Seco J, Palacín M, et al. Disruption of
868 mitochondrial dynamics triggers muscle inflammation through interorganellar contacts and
869 mitochondrial DNA mislocation. Nat Commun. 2023 Jan 6;14(1):108.

870 5. Zervopoulos SD, Boukouris AE, Saleme B, Haromy A, Tejay S, Sutendra G, et al. MFN2-driven
871 mitochondria-to-nucleus tethering allows a non-canonical nuclear entry pathway of the mitochondrial
872 pyruvate dehydrogenase complex. Mol Cell. 2022 Mar 3;82(5):1066-1077.e7.

873 6. Li J, Dang X, Franco A, Dorn GW. Reciprocal Regulation of Mitofusin 2-Mediated Mitophagy and
874 Mitochondrial Fusion by Different PINK1 Phosphorylation Events. Front Cell Dev Biol. 2022;10:868465.

875 7. McLelland GL, Goiran T, Yi W, Dorval G, Chen CX, Lauinger ND, et al. Mfn2 ubiquitination by
876 PINK1/parkin gates the p97-dependent release of ER from mitochondria to drive mitophagy. Dikic I,
877 editor. eLife. 2018 Apr 20;7:e32866.

878 8. Sharma G, Pfeffer G, Shutt TE. Genetic Neuropathy Due to Impairments in Mitochondrial
879 Dynamics. Biology. 2021 Apr;10(4):268.

880 9. Feely SME, Laura M, Siskind CE, Sottile S, Davis M, Gibbons VS, et al. MFN2 mutations cause
881 severe phenotypes in most patients with CMT2A. Neurology. 2011 May 17;76(20):1690–6.

882 10. Rouzier C, Bannwarth S, Chaussenot A, Chevrollier A, Verschueren A, Bonello-Palot N, et al. The
883 MFN2 gene is responsible for mitochondrial DNA instability and optic atrophy “plus” phenotype. Brain J
884 Neurol. 2012 Jan;135(Pt 1):23–34.

885 11. Abati E, Manini A, Velardo D, Del Bo R, Napoli L, Rizzo F, et al. Clinical and genetic features of a
886 cohort of patients with MFN2-related neuropathy. Sci Rep. 2022 Apr 13;12(1):6181.

887 12. Verhoeven K, Claeys KG, Züchner S, Schröder JM, Weis J, Ceuterick C, et al. MFN2 mutation
888 distribution and genotype/phenotype correlation in Charcot–Marie–Tooth type 2. Brain. 2006 Aug
889 1;129(8):2093–102.

890 13. Sharma G, Zaman M, Sabouny R, Joel M, Martens K, Martino D, et al. Characterization of a novel
891 variant in the HR1 domain of MFN2 in a patient with ataxia, optic atrophy and sensorineural hearing loss.
892 F1000Research. 2022 Sep 2;10:606.

893 14. Sawyer SL, Cheuk-Him Ng A, Innes AM, Wagner JD, Dyment DA, Tetreault M, et al. Homozygous
894 mutations in MFN2 cause multiple symmetric lipomatosis associated with neuropathy. Hum Mol Genet.
895 2015 Sep 15;24(18):5109–14.

896 15. Mann JP, Duan X, Patel S, Tábara LC, Scurria F, Alvarez-Guaita A, et al. A mouse model of human
897 mitofusin-2-related lipodystrophy exhibits adipose-specific mitochondrial stress and reduced leptin
898 secretion. eLife. 2023 Feb 1;12:e82283.

899 16. Masingue M, Vatier C, Jéru I, Latour P, Jardel C, Laforêt P, et al. Homozygous p.R707W MFN2
900 mutation is associated with neuropathy, lipomatosis, peripheral lipoatrophy and metabolic alterations.
901 Neuromuscul Disord. 2017 Oct 1;27:S148.

902 17. Zaman M, Shutt TE. The Role of Impaired Mitochondrial Dynamics in MFN2-Mediated Pathology.
903 Front Cell Dev Biol. 2022;10:858286.

904 18. Chen H, Vermulst M, Wang YE, Chomyn A, Prolla TA, McCaffery JM, et al. Mitochondrial fusion is
905 required for mtDNA stability in skeletal muscle and tolerance of mtDNA mutations. Cell. 2010 Apr
906 16;141(2):280–9.

907 19. Rodríguez-Nuevo A, Díaz-Ramos A, Noguera E, Díaz-Sáez F, Duran X, Muñoz JP, et al.
908 Mitochondrial DNA and TLR9 drive muscle inflammation upon Opa1 deficiency. EMBO J. 2018 May
909 15;37(10):e96553.

910 20. Sidarala V, Zhu J, Levi-D'Ancona E, Pearson GL, Reck EC, Walker EM, et al. Mitofusin 1 and 2
911 regulation of mitochondrial DNA content is a critical determinant of glucose homeostasis. Nat Commun.
912 2022 Apr 29;13(1):2340.

913 21. Vielhaber S, Debska-Vielhaber G, Peeva V, Schoeler S, Kudin AP, Minin I, et al. Mitofusin 2
914 mutations affect mitochondrial function by mitochondrial DNA depletion. Acta Neuropathol (Berl). 2013
915 Feb;125(2):245–56.

916 22. Newman LE, Shadel GS. Mitochondrial DNA Release in Innate Immune Signaling. Annu Rev
917 Biochem. 2023 Jun 20;92:299–332.

918 23. VanPortfliet JJ, Chute C, Lei Y, Shutt TE, West AP. Mitochondrial DNA release and sensing in
919 innate immune responses. Hum Mol Genet. 2024 May 22;33(R1):R80–91.

920 24. Al Khatib I, Deng J, Lei Y, Torres-Odio S, Rojas GR, Newman LE, et al. Activation of the cGAS-STING
921 innate immune response in cells with deficient mitochondrial topoisomerase TOP1MT. Hum Mol Genet.
922 2023 Jul 20;32(15):2422–40.

923 25. Kim J, Kim HS, Chung JH. Molecular mechanisms of mitochondrial DNA release and activation of
924 the cGAS-STING pathway. Exp Mol Med. 2023 Mar;55(3):510–9.

925 26. Pereira CA, Carlos D, Ferreira NS, Silva JF, Zanotto CZ, Zamboni DS, et al. Mitochondrial DNA
926 Promotes NLRP3 Inflammasome Activation and Contributes to Endothelial Dysfunction and Inflammation
927 in Type 1 Diabetes. Front Physiol. 2019;10:1557.

928 27. Qiu Y, Huang Y, Chen M, Yang Y, Li X, Zhang W. Mitochondrial DNA in NLRP3 inflammasome
929 activation. Int Immunopharmacol. 2022 Jul;108:108719.

930 28. Martens K, Leckie J, Fok D, Wells RA, Chhibber S, Pfeffer G. Case Report: Calpainopathy
931 Presenting After Bone Marrow Transplantation, With Studies of Donor Genetic Content in Various Tissue
932 Types. Front Neurol. 2020;11:604547.

933 29. Griffin HR, Pyle A, Blakely EL, Alston CL, Duff J, Hudson G, et al. Accurate mitochondrial DNA
934 sequencing using off-target reads provides a single test to identify pathogenic point mutations. Genet
935 Med. 2014 Dec;16(12):962–71.

936 30. Di Tommaso P, Moretti S, Xenarios I, Orobitg M, Montanyola A, Chang JM, et al. T-Coffee: a web
937 server for the multiple sequence alignment of protein and RNA sequences using structural information
938 and homology extension. Nucleic Acids Res. 2011 Jul;39(Web Server issue):W13-17.

939 31. UniProt Consortium. UniProt: the Universal Protein Knowledgebase in 2023. Nucleic Acids Res.
940 2023 Jan 6;51(D1):D523–31.

941 32. Schindelin J, Arganda-Carreras I, Frise E, Kaynig V, Longair M, Pietzsch T, et al. Fiji: an open-
942 source platform for biological-image analysis. Nat Methods. 2012 Jun 28;9(7):676–82.

943 33. Uddin GM, Lacroix R, Zaman M, Khatib IA, Rho JM, Kurrasch DM, et al. The Ketogenic Diet
944 Metabolite β-Hydroxybutyrate Promotes Mitochondrial Elongation via Deacetylation and Improves
945 Autism-like Behavior in Zebrafish. bioRxiv. 2022 Jan 1;2022.10.03.510695.

946 34. Zhao T, Goedhart CM, Sam PN, Sabouny R, Lingrell S, Cornish AJ, et al. PISD is a mitochondrial
947 disease gene causing skeletal dysplasia, cataracts, and white matter changes. Life Sci Alliance. 2019
948 Apr;2(2):e201900353.

949 35. Al Khatib I, Deng J, Symes A, Kerr M, Zhang H, Huang SYN, et al. Functional characterization of
950 two variants of mitochondrial topoisomerase TOP1MT that impact regulation of the mitochondrial
951 genome. J Biol Chem. 2022 Oct;298(10):102420.

952 36. Valente AJ, Maddalena LA, Robb EL, Moradi F, Stuart JA. A simple ImageJ macro tool for
953 analyzing mitochondrial network morphology in mammalian cell culture. Acta Histochem. 2017
954 Apr;119(3):315–26.

955 37. Bolte S, Cordelières FP. A guided tour into subcellular colocalization analysis in light microscopy. J
956 Microsc. 2006 Dec;224(Pt 3):213–32.

957 38. Montava-Garriga L, Singh F, Ball G, Ganley IG. Semi-automated quantitation of mitophagy in cells
958 and tissues. Mech Ageing Dev. 2020 Jan;185:111196.

959 39. Zhang Q, Bethmann C, Worth NF, Davies JD, Wasner C, Feuer A, et al. Nesprin-1 and -2 are
960 involved in the pathogenesis of Emery Dreifuss muscular dystrophy and are critical for nuclear envelope
961 integrity. Hum Mol Genet. 2007 Dec 1;16(23):2816–33.

962 40. Beręsewicz M, Boratyńska-Jasińska A, Charzewski Ł, Kawalec M, Kabzińska D, Kochański A, et al.
963 The Effect of a Novel c.820C>T (Arg274Trp) Mutation in the Mitofusin 2 Gene on Fibroblast Metabolism
964 and Clinical Manifestation in a Patient. PloS One. 2017;12(1):e0169999.

965 41. Sabouny R, Shutt TE. The role of mitochondrial dynamics in mtDNA maintenance. J Cell Sci. 2021
966 Dec 15;134(24):jcs258944.

967 42. de Brito OM, Scorrano L. Mitofusin 2 tethers endoplasmic reticulum to mitochondria. Nature.
968 2008 Dec 4;456(7222):605–10.

969 43. Rambold AS, Cohen S, Lippincott-Schwartz J. Fatty acid trafficking in starved cells: regulation by
970 lipid droplet lipolysis, autophagy, and mitochondrial fusion dynamics. Dev Cell. 2015 Mar 23;32(6):678–
971 92.

972 44. Yasuda H, Leelahavanichkul A, Tsunoda S, Dear JW, Takahashi Y, Ito S, et al. Chloroquine and
973 inhibition of Toll-like receptor 9 protect from sepsis-induced acute kidney injury. Am J Physiol Renal
974 Physiol. 2008 May;294(5):F1050–8.

975 45. Vincent J, Adura C, Gao P, Luz A, Lama L, Asano Y, et al. Small molecule inhibition of cGAS
976 reduces interferon expression in primary macrophages from autoimmune mice. Nat Commun. 2017 Sep
977 29;8(1):750.

978 46. Huang P, Yu T, Yoon Y. Mitochondrial clustering induced by overexpression of the mitochondrial
979 fusion protein Mfn2 causes mitochondrial dysfunction and cell death. Eur J Cell Biol. 2007 Jun;86(6):289–
980 302.

981 47. Pipis M, Feely SME, Polke JM, Skorupinska M, Perez L, Shy RR, et al. Natural history of Charcot-
982 Marie-Tooth disease type 2A: a large international multicentre study. Brain J Neurol. 2020 Dec
983 1;143(12):3589–602.

984 48. Xie Y, Li X, Liu L, Hu Z, Huang S, Zhan Y, et al. MFN2-related genetic and clinical features in a
985 cohort of Chinese CMT2 patients. J Peripher Nerv Syst JPNS. 2016 Mar;21(1):38–44.

986 49. Tarailo-Graovac M, Zhu JYA, Matthews A, van Karnebeek CDM, Wasserman WW. Assessment of
987 the ExAC data set for the presence of individuals with pathogenic genotypes implicated in severe
988 Mendelian pediatric disorders. Genet Med Off J Am Coll Med Genet. 2017 Dec;19(12):1300–8.

989 50. Almomen M, Martens K, Quadir A, Pontifex CS, Hanson A, Korngut L, et al. High diagnostic yield
990 and novel variants in very late-onset spasticity. J Neurogenet. 2019 Mar;33(1):27–32.

991 51. Sabouny R, Shutt TE. Reciprocal Regulation of Mitochondrial Fission and Fusion. Trends Biochem
992 Sci. 2020 Jul;45(7):564–77.

993 52. Filipe A, Chernorudskiy A, Arbogast S, Varone E, Villar-Quiles RN, Pozzer D, et al. Defective
994 endoplasmic reticulum-mitochondria contacts and bioenergetics in SEPN1-related myopathy. Cell Death
995 Differ. 2021 Jan;28(1):123.

996 53. Larrea D, Pera M, Gonnelli A, Quintana-Cabrera R, Akman HO, Guardia-Laguarta C, et al. MFN2
997 mutations in Charcot-Marie-Tooth disease alter mitochondria-associated ER membrane function but do
998 not impair bioenergetics. Hum Mol Genet. 2019 Jun 1;28(11):1782–800.

999 54. Boutant M, Kulkarni SS, Joffraud M, Ratajczak J, Valera-Alberni M, Combe R, et al. Mfn2 is critical
1000 for brown adipose tissue thermogenic function. EMBO J. 2017 Jun 1;36(11):1543–58.

1001 55. Rodríguez-Nuevo A, Díaz-Ramos A, Noguera E, Díaz-Sáez F, Duran X, Muñoz JP, et al.
1002 Mitochondrial DNA and TLR9 drive muscle inflammation upon Opa1 deficiency. EMBO J. 2018 May
1003 15;37(10):e96553.

1004 56. Wei FL, Wang TF, Wang CL, Zhang ZP, Zhao JW, Heng W, et al. Cytoplasmic Escape of
1005 Mitochondrial DNA Mediated by Mfn2 Downregulation Promotes Microglial Activation via cGas-Sting
1006 Axis in Spinal Cord Injury. Adv Sci Weinh Baden-Wurtt Ger. 2023 Nov 27;e2305442.

1007 57. Zhou M, Cheng X, Zhu W, Jiang J, Zhu S, Wu X, et al. Activation of cGAS-STING pathway - A
1008 possible cause of myofiber atrophy/necrosis in dermatomyositis and immune-mediated necrotizing
1009 myopathy. J Clin Lab Anal. 2022 Oct;36(10):e24631.

1010 58. Sen A, Boix J, Pla-Martín D. Endosomal-dependent mitophagy coordinates mitochondrial
1011 nucleoid and mtDNA elimination. Autophagy. 19(9):2609–10.

1012 59. Sen A, Kallabis S, Gaedke F, Jüngst C, Boix J, Nüchel J, et al. Mitochondrial membrane proteins
1013 and VPS35 orchestrate selective removal of mtDNA. Nat Commun. 2022 Nov 7;13:6704.

1014 60. Newman LE, Weiser Novak S, Rojas GR, Tadepalle N, Schiavon CR, Grotjahn DA, et al.
1015 Mitochondrial DNA replication stress triggers a pro-inflammatory endosomal pathway of nucleoid
1016 disposal. Nat Cell Biol. 2024 Feb;26(2):194–206.

1017 61. Silva Ramos E, Motori E, Brüser C, Kühl I, Yeroslaviz A, Ruzzenente B, et al. Mitochondrial fusion
1018 is required for regulation of mitochondrial DNA replication. PLoS Genet. 2019 Jun;15(6):e1008085.

1019 62. Ilamathi HS, Benhammouda S, Lounas A, Al-Naemi K, Desrochers-Goyette J, Lines MA, et al.
1020 Contact sites between endoplasmic reticulum sheets and mitochondria regulate mitochondrial DNA
1021 replication and segregation. iScience. 2023 Jul 21;26(7):107180.

1022 63. Lewis SC, Uchiyama LF, Nunnari J. ER-mitochondria contacts couple mtDNA synthesis with
1023 mitochondrial division in human cells. Science. 2016 Jul 15;353(6296):aaf5549.

1024 64. Tur J, Pereira-Lopes S, Vico T, Marín EA, Muñoz JP, Hernández-Alvarez M, et al. Mitofusin 2 in
1025 Macrophages Links Mitochondrial ROS Production, Cytokine Release, Phagocytosis, Autophagy, and
1026 Bactericidal Activity. Cell Rep. 2020 Aug 25;32(8):108079.

1027 65. Liu H, Liu X, Zhuang H, Fan H, Zhu D, Xu Y, et al. Mitochondrial Contact Sites in Inflammation-
1028 Induced Cardiovascular Disease. Front Cell Dev Biol. 2020 Jul 30;8:692.

1029 66. Akhmetova K, Balasov M, Chesnokov I. Drosophila STING protein has a role in lipid metabolism.
1030 eLife. 2021 Sep 1;10:e67358.

1031 67. Bai J, Cervantes C, He S, He J, Plasko GR, Wen J, et al. Mitochondrial stress-activated cGAS-STING
1032 pathway inhibits thermogenic program and contributes to overnutrition-induced obesity in mice.
1033 Commun Biol. 2020 May 22;3(1):257.

1034 68. Monson EA, Crosse KM, Das M, Helbig KJ. Lipid droplet density alters the early innate immune
1035 response to viral infection. Zhang L, editor. PLOS ONE. 2018 Jan 2;13(1):e0190597.

1036 69. Boucher DM, Vijithakumar V, Ouimet M. Lipid Droplets as Regulators of Metabolism and
1037 Immunity. Immunometabolism [Internet]. 2021 Jul [cited 2024 Feb 19];3(3). Available from:
1038 https://journals.lww.com/10.20900/immunometab20210021

1039 70. Chen H, Vermulst M, Wang YE, Chomyn A, Prolla TA, McCaffery JM, et al. Mitochondrial fusion is
1040 required for mtDNA stability in skeletal muscle and tolerance of mtDNA mutations. Cell. 2010 Apr
1041 16;141(2):280–9.

1042 71. Chen Z, Bordieanu B, Kesavan R, Lesner NP, Venigalla SSK, Shelton SD, et al. Lactate metabolism
1043 is essential in early-onset mitochondrial myopathy. Sci Adv. 2023 Jan 4;9(1):eadd3216.

1044 72. Franco A, Li J, Kelly DP, Hershberger RE, Marian AJ, Lewis RM, et al. A human mitofusin 2
1045 mutation can cause mitophagic cardiomyopathy. eLife. 2023 Nov 1;12:e84235.

1046 73. Sebastián D, Sorianello E, Segalés J, Irazoki A, Ruiz-Bonilla V, Sala D, et al. Mfn2 deficiency links
1047 age-related sarcopenia and impaired autophagy to activation of an adaptive mitophagy pathway. EMBO
1048 J. 2016 Aug 1;35(15):1677–93.

1049 74. Hines TJ, Bailey J, Liu H, Guntur AR, Seburn KL, Pratt SL, et al. A Novel ENU-Induced Mfn2
1050 Mutation Causes Motor Deficits in Mice without Causing Peripheral Neuropathy. Biology. 2023 Jul
1051 3;12(7):953.

1052 75. Perandini LA, Chimin P, Lutkemeyer D da S, Câmara NOS. Chronic inflammation in skeletal muscle
1053 impairs satellite cells function during regeneration: can physical exercise restore the satellite cell niche?
1054 FEBS J. 2018 Jun;285(11):1973–84.

1055 76. Chandran R, Knobloch TJ, Anghelina M, Agarwal S. Biomechanical signals upregulate myogenic
1056 gene induction in the presence or absence of inflammation. Am J Physiol Cell Physiol. 2007
1057 Jul;293(1):C267-276.

1058 77. Cai D, Frantz JD, Tawa NE, Melendez PA, Oh BC, Lidov HGW, et al. IKKbeta/NF-kappaB activation
1059 causes severe muscle wasting in mice. Cell. 2004 Oct 15;119(2):285–98.

1060 78. Lundberg IE, Fujimoto M, Vencovsky J, Aggarwal R, Holmqvist M, Christopher-Stine L, et al.
1061 Idiopathic inflammatory myopathies. Nat Rev Dis Primer. 2021 Dec 2;7(1):86.

1062 79. Silva AMS, Campos ED, Zanoteli E. Inflammatory myopathies: an update for neurologists. Arq
1063 Neuropsiquiatr. 2022 May;80(5 Suppl 1):238–48.

1064 80. Stavropoulos F, Sargiannidou I, Potamiti L, Kagiava A, Panayiotidis MI, Bae JH, et al. Aberrant
1065 Mitochondrial Dynamics and Exacerbated Response to Neuroinflammation in a Novel Mouse Model of
1066 CMT2A. Int J Mol Sci. 2021 Oct 26;22(21):11569.

1067 81. Kerckhove N, Pezet D, Balayssac D. Long-Term Effects, Pathophysiological Mechanisms, and Risk
1068 Factors of Chemotherapy-Induced Peripheral Neuropathies: A Comprehensive Literature Review. Front
1069 Pharmacol [Internet]. 2017 Feb 24 [cited 2024 Mar 12];8. Available from:
1070 https://www.frontiersin.org/journals/pharmacology/articles/10.3389/fphar.2017.00086/full

1071 82. Rivera DR, Ganz PA, Weyrich MS, Bandos H, Melnikow J. Chemotherapy-Associated Peripheral
1072 Neuropathy in Patients With Early-Stage Breast Cancer: A Systematic Review. JNCI J Natl Cancer Inst.
1073 2018 Feb 1;110(2):djx140.

1074 83. Jones MR, Urits I, Wolf J, Corrigan D, Colburn L, Peterson E, et al. Drug-Induced Peripheral
1075 Neuropathy: A Narrative Review. Curr Clin Pharmacol. 2020 Apr;15(1):38.

1076 84. Grisold W, Cavaletti G, Windebank AJ. Peripheral neuropathies from chemotherapeutics and
1077 targeted agents: diagnosis, treatment, and prevention. Neuro-Oncol. 2012 Sep;14(Suppl 4):iv45–54.

1078 85. Cella D, Huang H, Homesley HD, Montag A, Salani R, De Geest K, et al. Patient-reported
1079 peripheral neuropathy of doxorubicin and cisplatin with and without paclitaxel in the treatment of
1080 advanced endometrial cancer: Results from GOG 184. Gynecol Oncol. 2010 Dec;119(3):538–42.

1081 86. Wu Z, Oeck S, West AP, Mangalhara KC, Sainz AG, Newman LE, et al. Mitochondrial DNA Stress
1082 Signalling Protects the Nuclear Genome. Nat Metab. 2019 Dec;1(12):1209–18.

1083

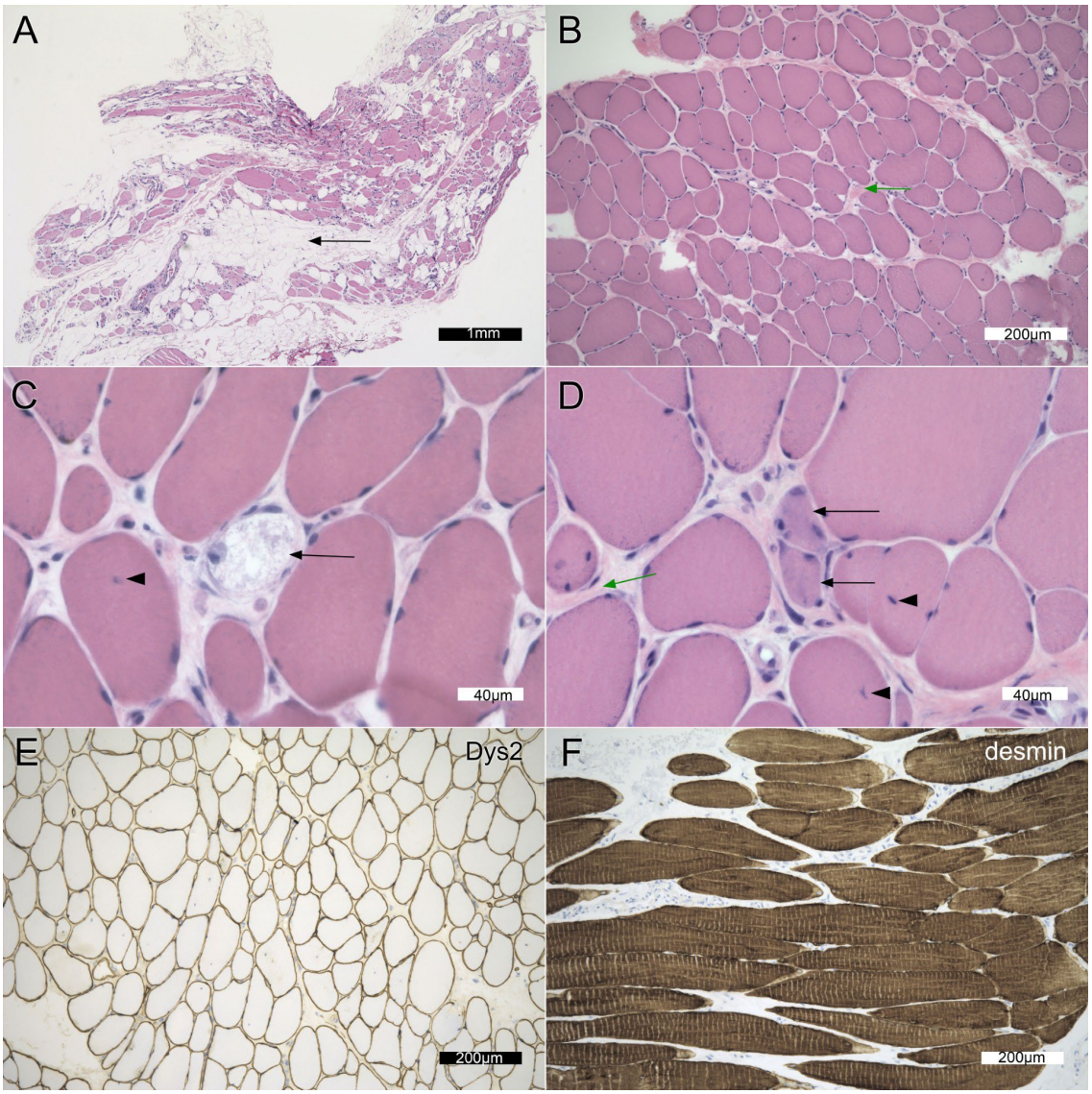
A
1mm
B
200µm
C
40µm
D
40µm
E
Dys2
200µm
F
desmin
200µm

G

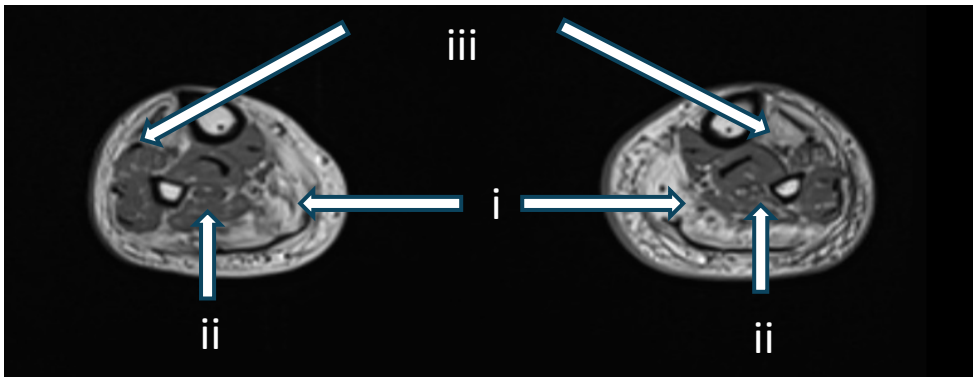
iii
i
ii
ii

H

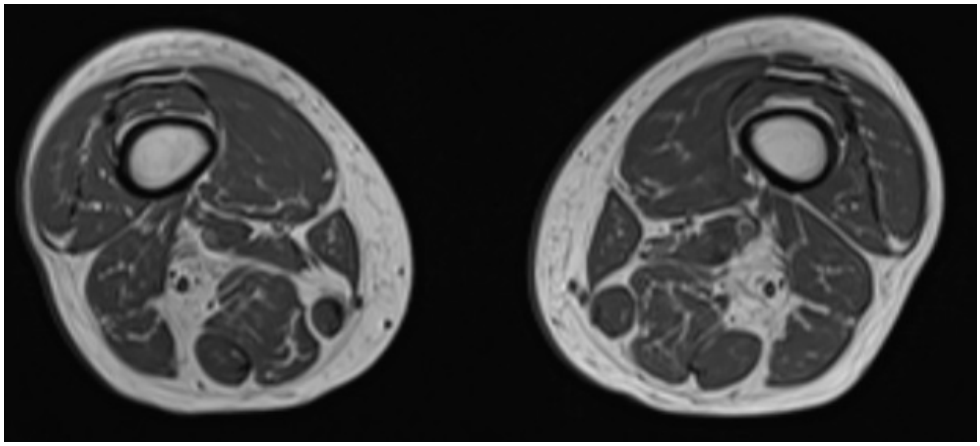

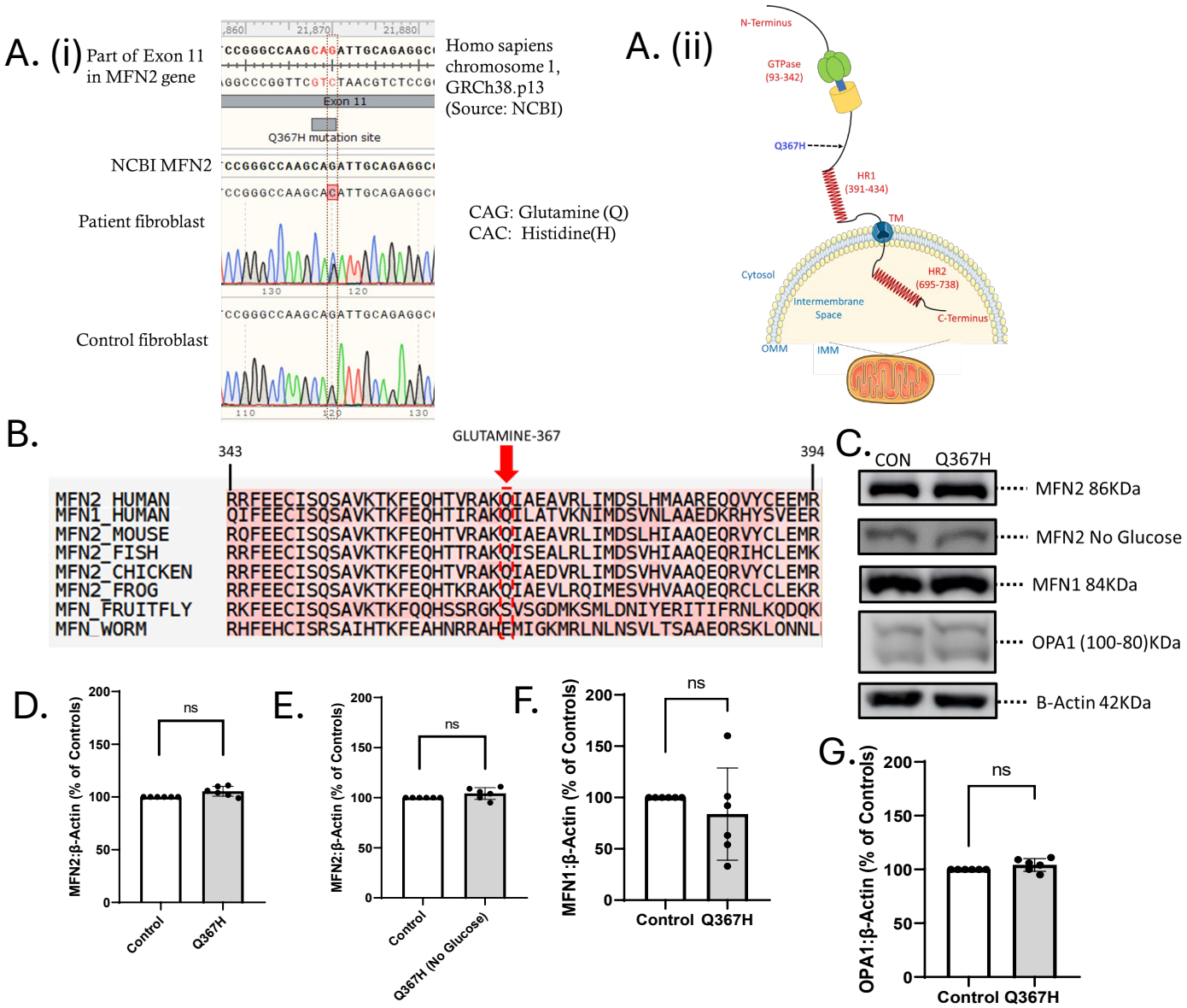
A. (i)
Part of Exon 11 in MFN2 gene
Homo sapiens chromosome 1, GRCh38.p13 (Source: NCBI)
Exon 11
Q367H mutation site
NCBI MFN2
Patient fibroblast
Control fibroblast
CAG: Glutamine (Q)
CAC: Histidine(H)
A. (ii)
N-Terminus
GTPase (93-342)
Q367H
HR1 (391-434)
TM
Cytosol
HR2 (695-738)
Intermembrane Space
C-Terminus
OMM
IMM
B.
GLUTAMINE-367
343
394
MFN2_HUMAN RRFEECISQSAVKTKFEQHTVRAKQIAEAVRLIMDSLHMAAREQQVYCEEMR
MFN1_HUMAN QIFEECISQSAVKTKFEQHTIRAKQILATVKNIMDSVNLAAEDKRHYSVEER
MFN2_MOUSE RQFEECISQSAVKTKFEQHTVRAKQIAEAVRLIMDSLHIAAQEQRVYCLEMR
MFN2_FISH RRFEECISQSAVKTKFEQHTTRAKQISEALRLIMDSVHIAAQEQRIHCLEMK
MFN2_CHICKEN RRFEECISQSAVKTKFEQHTVRAKQIAEDVRLIMDSVHVAAQEQRVYCLEMR
MFN2_FROG RRFEECISQSAVKTKFEQHTKRAKQIAEVLRQIMESVHVAAQEQRCLCLEKR
MFN_FRUITFLY RKFEECISQSAVKTKFQQHSSRGKSVSGDMKSMLDNIYERITIFRNLKQDQK
MFN_WORM RHFEHCISRSAIHTKFEAHNRRAHEMIGKMRLNLNSVLTSAAEQRSKLONNL
C.
CON
Q367H
MFN2 86KDa
MFN2 No Glucose
MFN1 84KDa
OPA1 (100-80)KDa
B-Actin 42KDa
D.
MFN2:β-Actin (% of Controls)
ns
Control
Q367H
E.
MFN2:β-Actin (% of Controls)
ns
Control
Q367H (No Glucose)
F.
MFN1:β-Actin (% of Controls)
ns
Control
Q367H
G.
OPA1:β-Actin (% of Controls)
ns
Control
Q367H

A.

Glucose Media

Control

Q367H

Glucose-Free Media

Control

Q367H

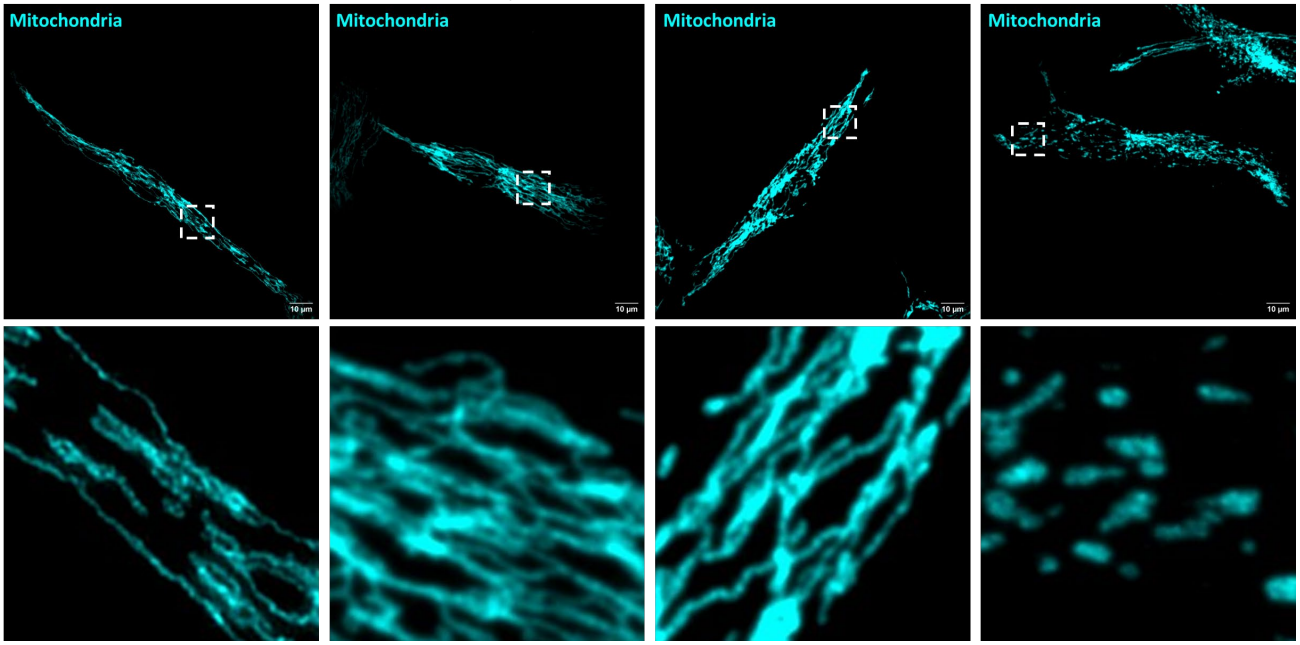

B.

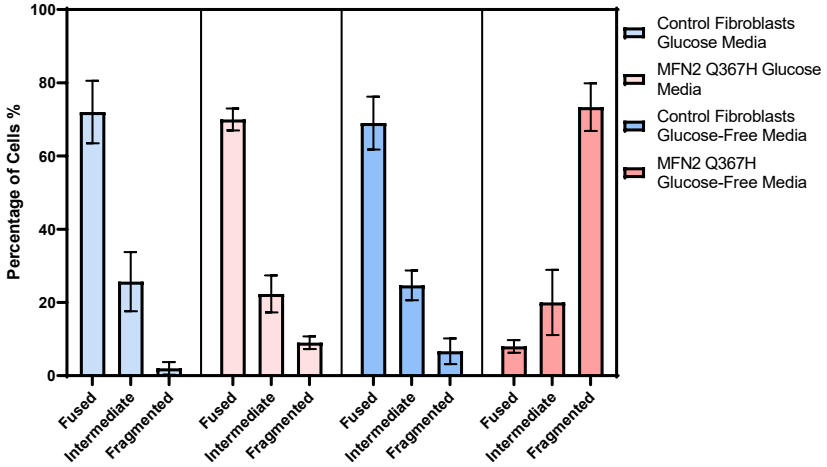

C.

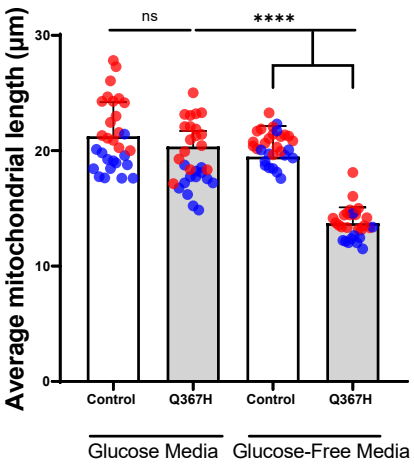

D.

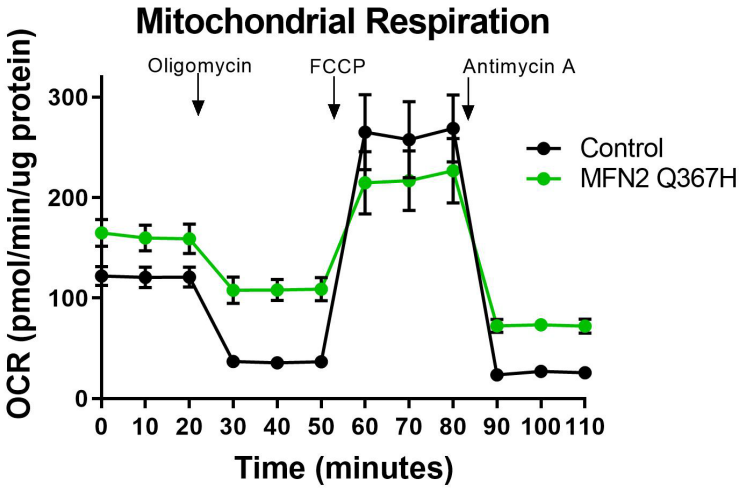

E.

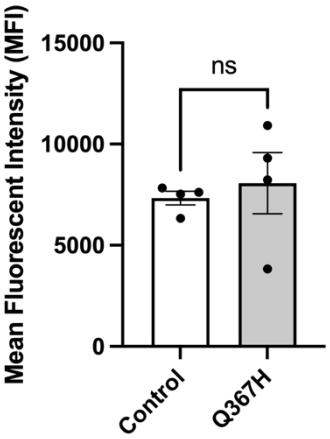

A.

Glucose Media | Glucose-Free Media

Control | Q367H | Control | Q367H

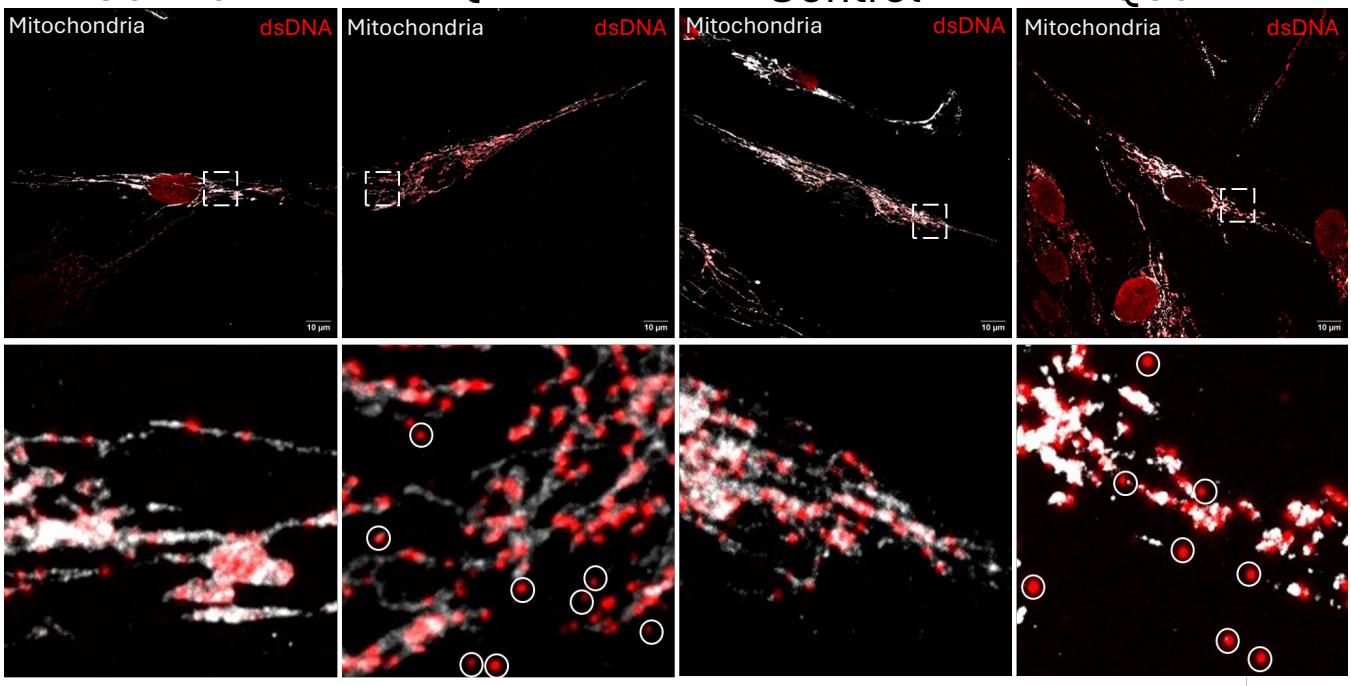

B.

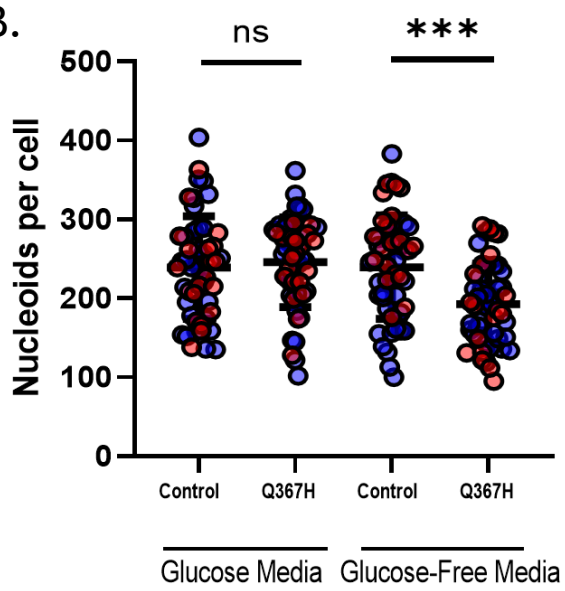

C.

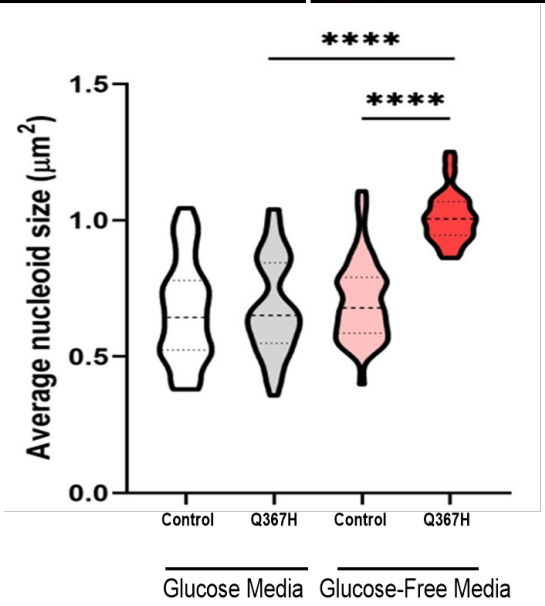

D.

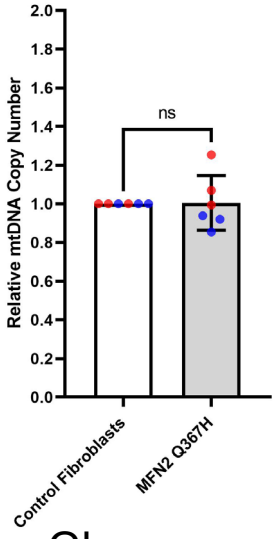

Glucose Media

E.

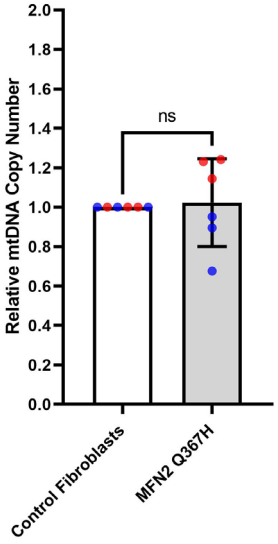

No Glucose Media

F.

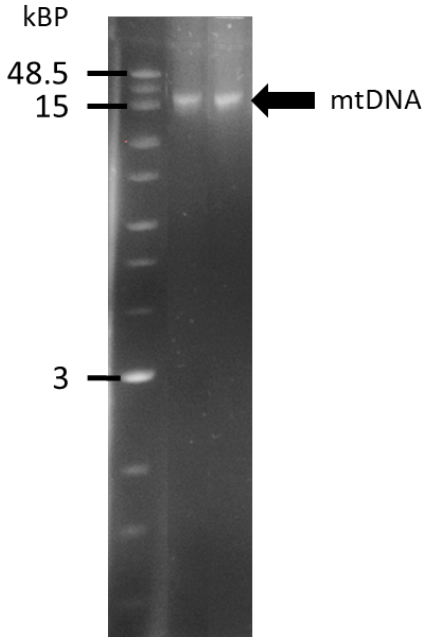

A.

GLUCOSE MEDIA | GLUCOSE-FREE MEDIA

Control | MFN2 Q367H | Control | MFN2 Q367H

Mitochondria
ER
MERCs
Inset
Merge

B.

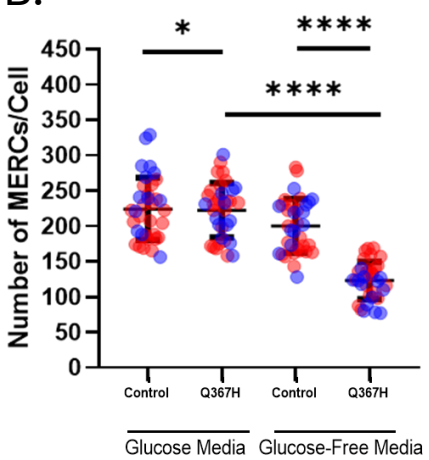

C.

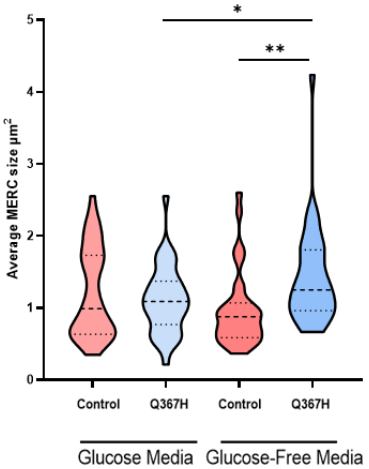

D.

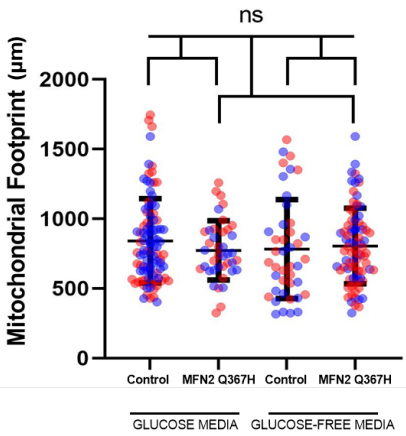

E.

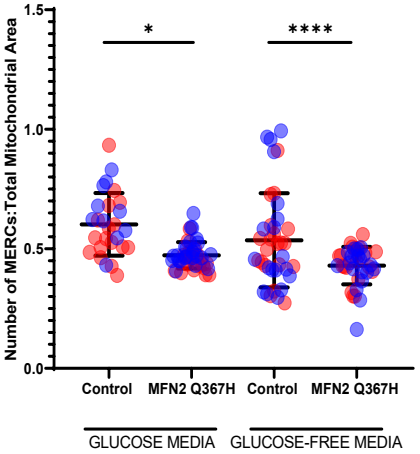

A.

Glucose Media

Control

Q367H

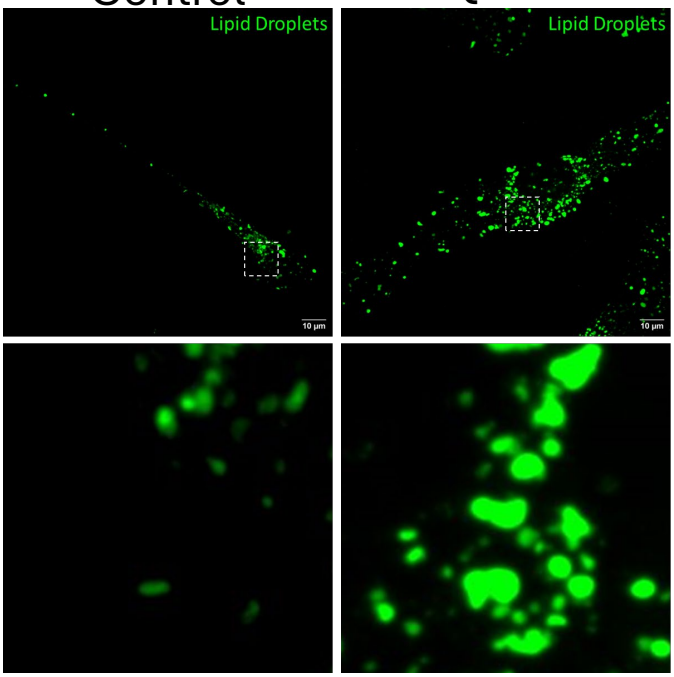

B.

Glucose-Free Media

Control

Q367H

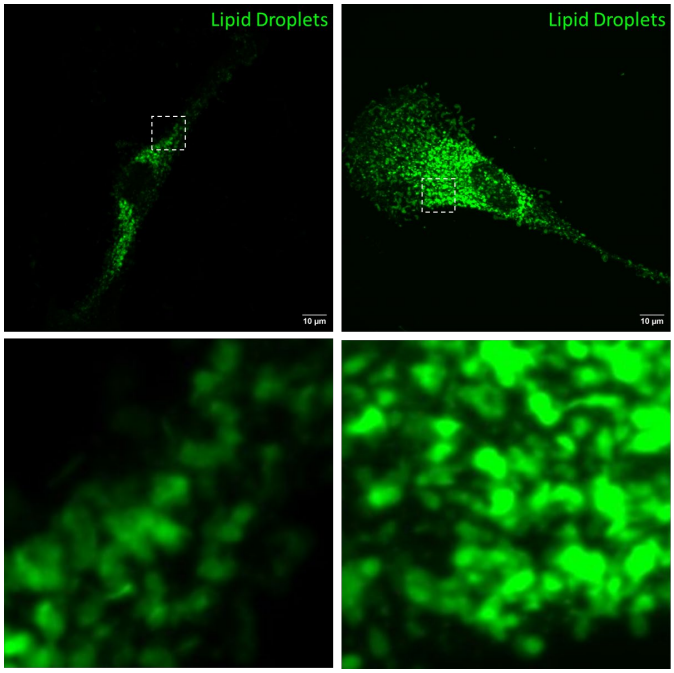

C.

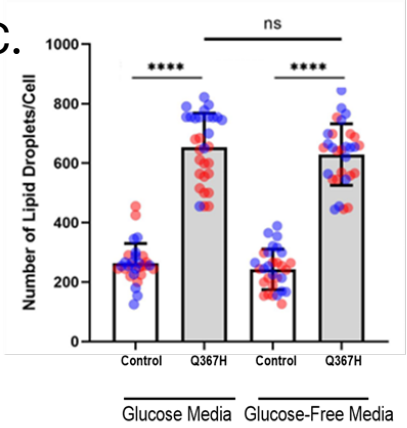

D.

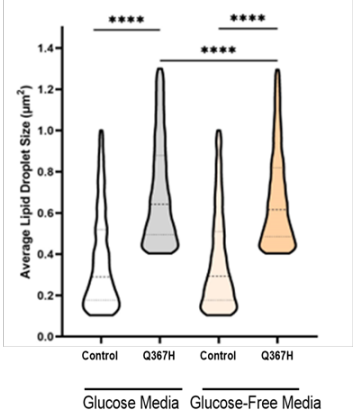

E.

Standard Media

Starvation Media

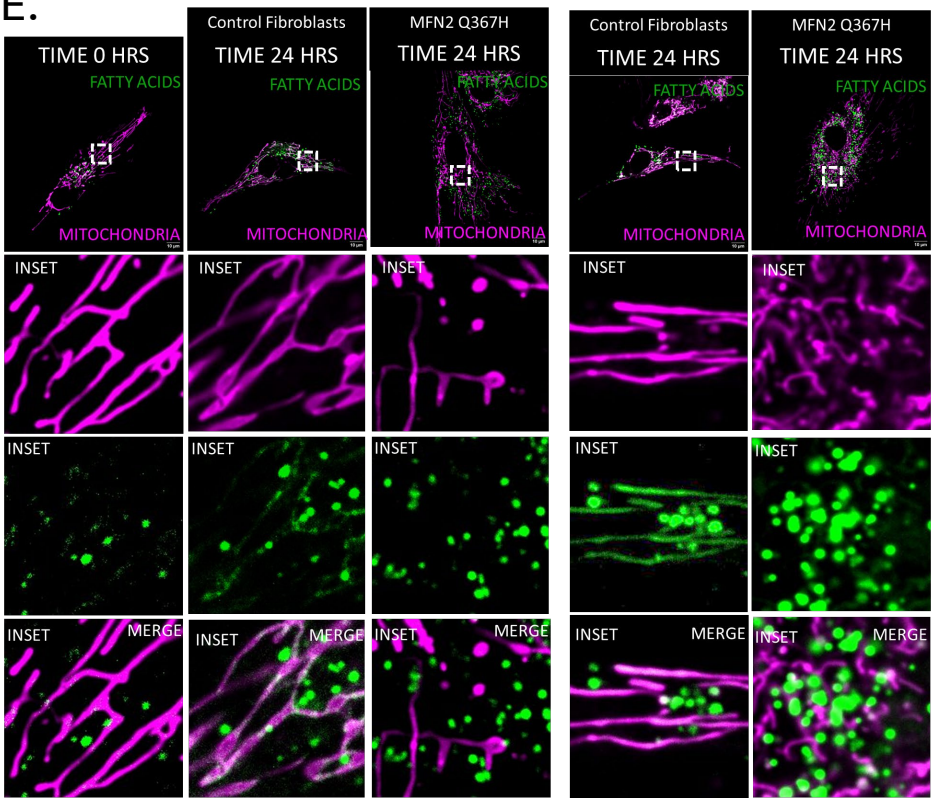

F.

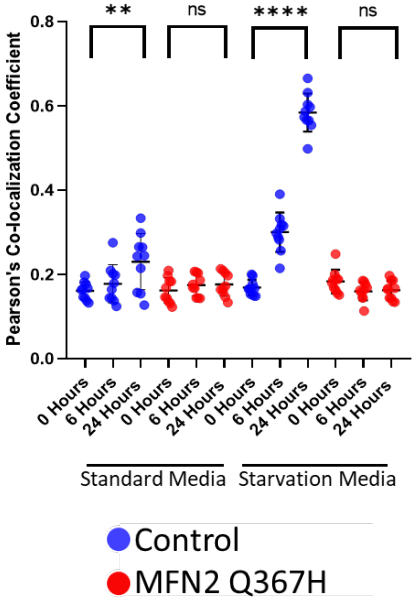

A.

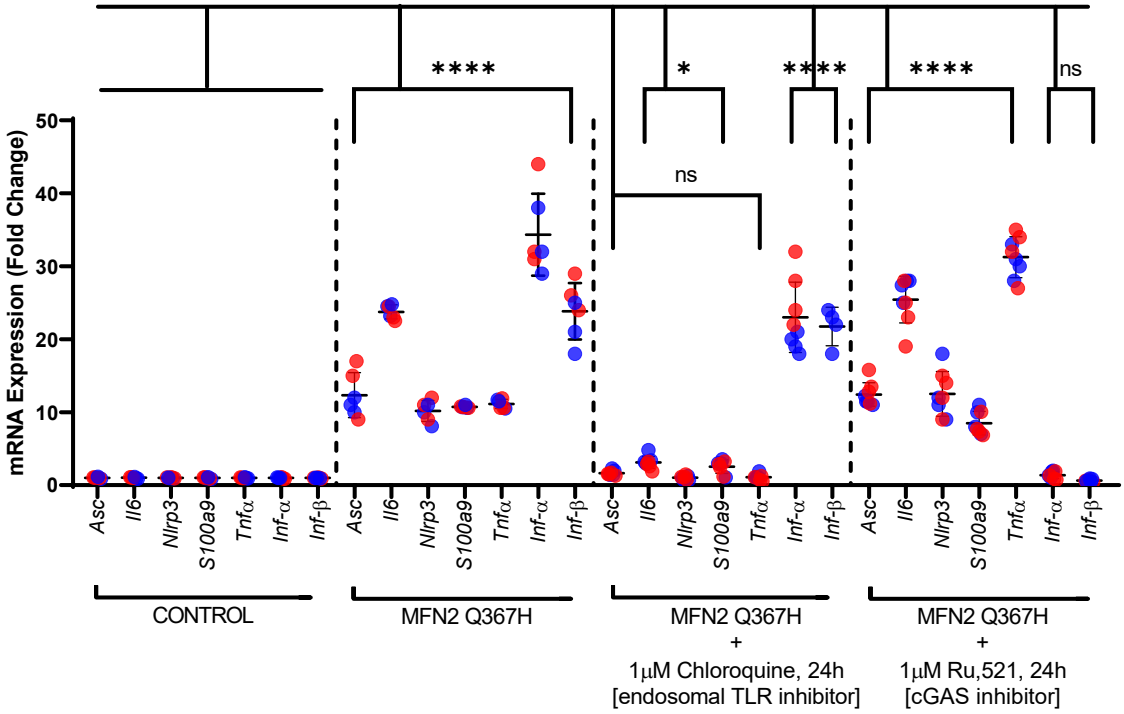
****
*
****
****
ns
ns
mRNA Expression (Fold Change)
50
40
30
20
10
0
Asc
Il6
Nlrp3
S100a9
Tnfα
Inf-α
Inf-β
CONTROL
MFN2 Q367H
MFN2 Q367H
+
1μM Chloroquine, 24h
[endosomal TLR inhibitor]
MFN2 Q367H
+
1μM Ru,521, 24h
[cGAS inhibitor]

B.

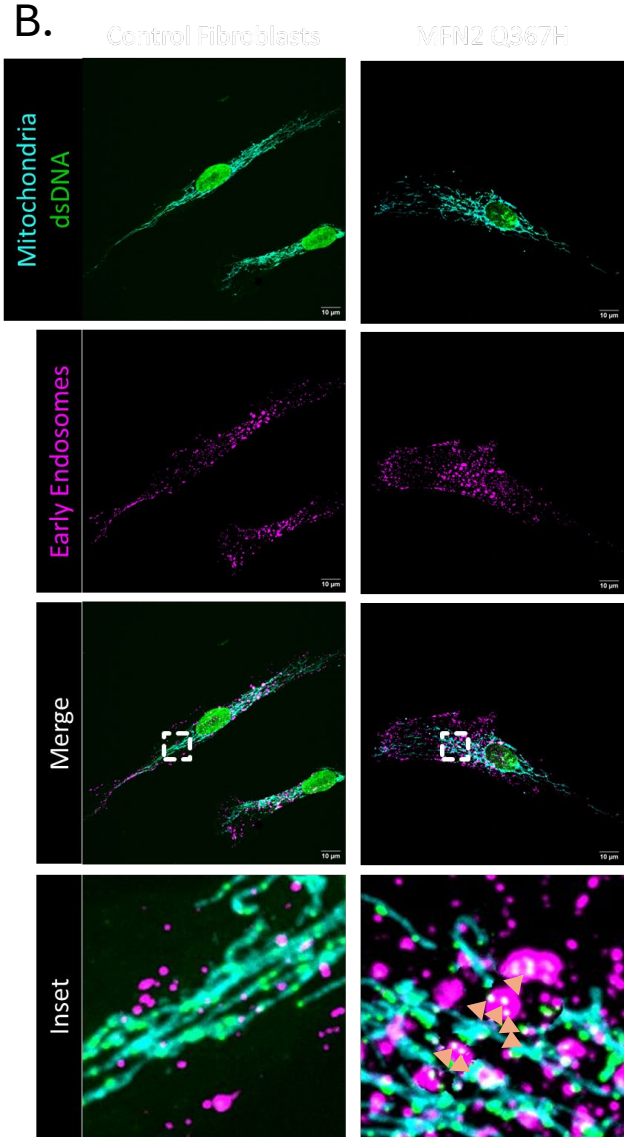
Control Fibroblasts
MFN2 Q367H
Mitochondria
dsDNA
Early Endosomes
Merge
Inset

C.

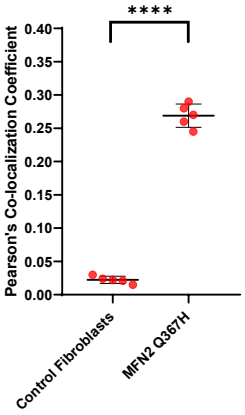
****
Pearson's Co-localization Coefficient
0.40
0.35
0.30
0.25
0.20
0.15
0.10
0.05
0.00
Control Fibroblasts
MFN2 Q367H

D.

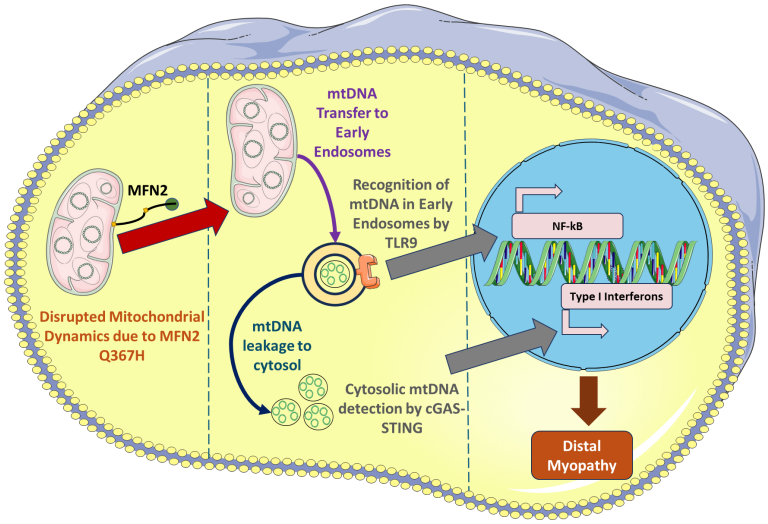
MFN2
Disrupted Mitochondrial Dynamics due to MFN2 Q367H
mtDNA Transfer to Early Endosomes
Recognition of mtDNA in Early Endosomes by TLR9
mtDNA leakage to cytosol
Cytosolic mtDNA detection by cGAS-STING
NF-kB
Type I Interferons
Distal Myopathy

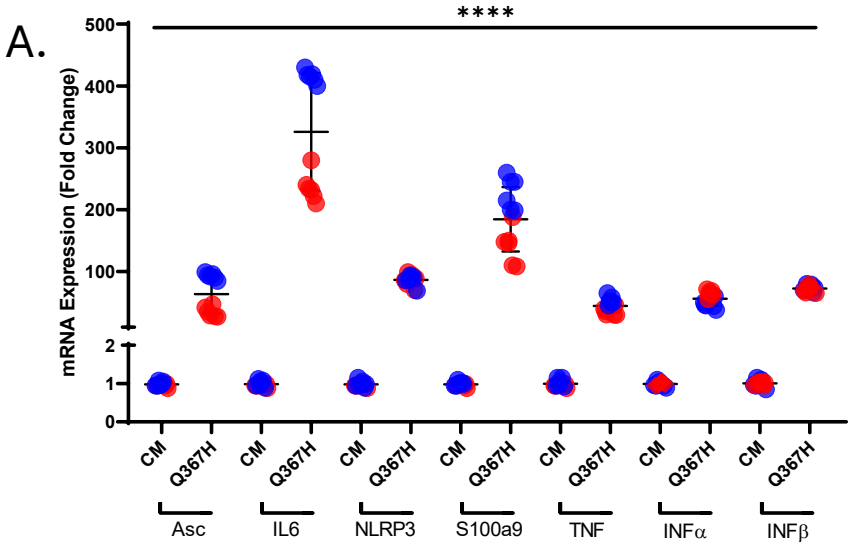
A.
****
mRNA Expression (Fold Change)
500
400
300
200
100
2
1
0
CM
Q367H
Asc
IL6
NLRP3
S100a9
TNF
INFα
INFβ

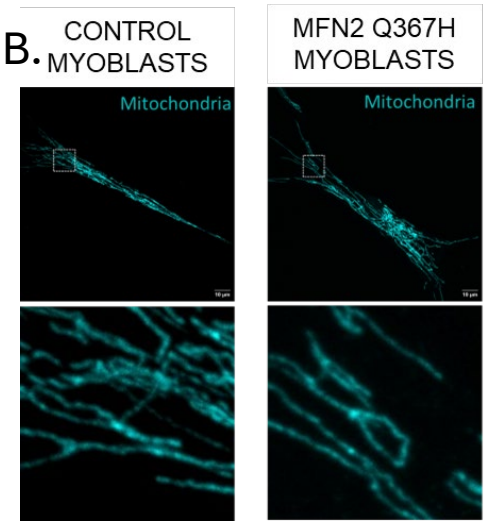
B.
CONTROL MYOBLASTS
MFN2 Q367H MYOBLASTS
Mitochondria
Mitochondria

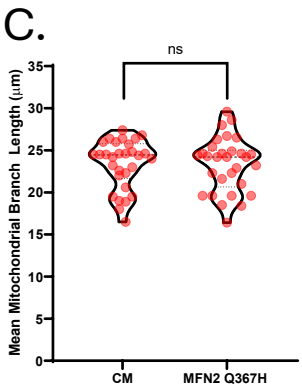
C.
ns
Mean Mitochondrial Branch Length (μm)
35
30
25
20
15
10
5
0
CM
MFN2 Q367H

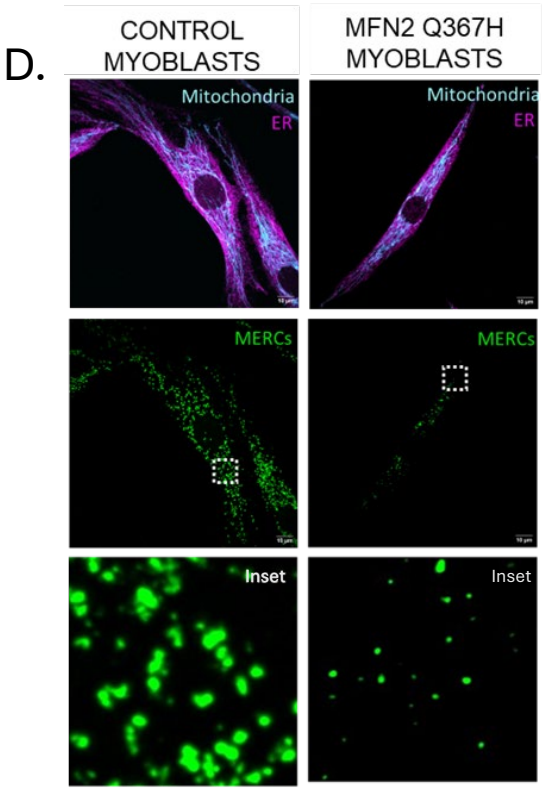
D.
CONTROL MYOBLASTS
MFN2 Q367H MYOBLASTS
Mitochondria
ER
Mitochondria
ER
MERCs
MERCs
Inset
Inset

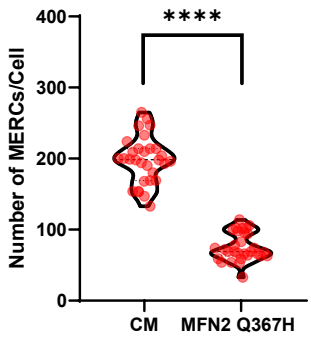
E.
****
Number of MERCs/Cell
400
300
200
100
0
CM
MFN2 Q367H

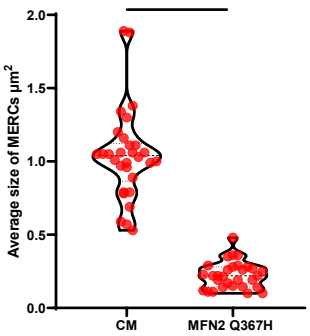
F.
****
Average size of MERCs μm²
2.0
1.5
1.0
0.5
0.0
CM
MFN2 Q367H

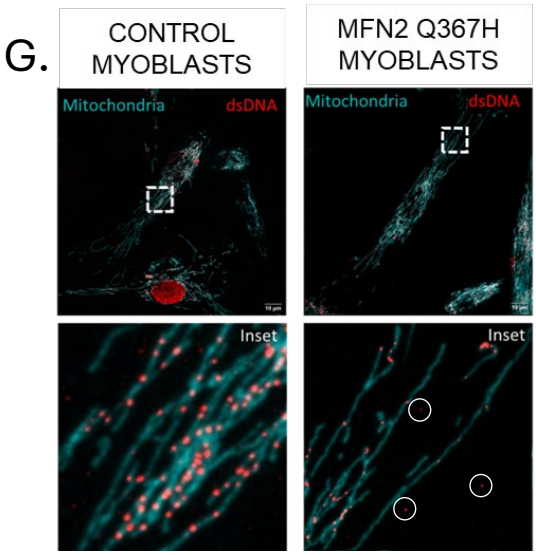
G.
CONTROL MYOBLASTS
MFN2 Q367H MYOBLASTS
Mitochondria
dsDNA
Mitochondria
dsDNA
Inset
Inset

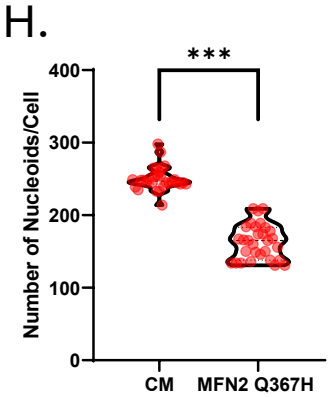
H.
***
Number of Nucleoids/Cell
400
300
200
100
0
CM
MFN2 Q367H

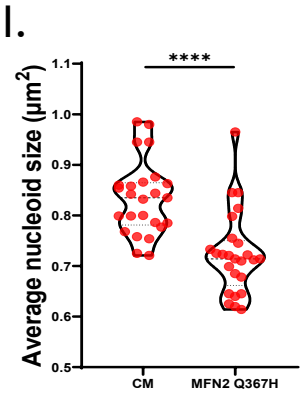
I.
****
Average nucleoid size (μm²)
1.1
1.0
0.9
0.8
0.7
0.6
0.5
CM
MFN2 Q367H

A.

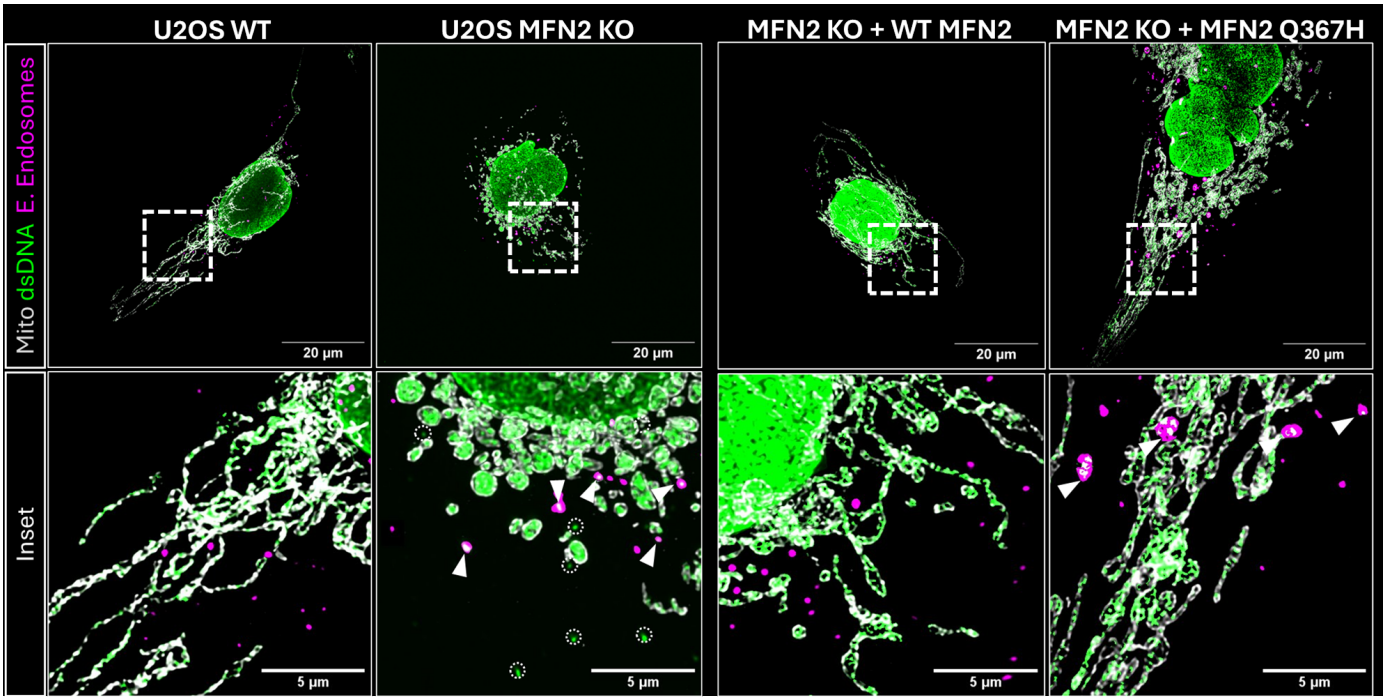
U2OS WT
U2OS MFN2 KO
MFN2 KO + WT MFN2
MFN2 KO + MFN2 Q367H
Mito dsDNA E. Endosomes
Inset
20 µm
5 µm

B.

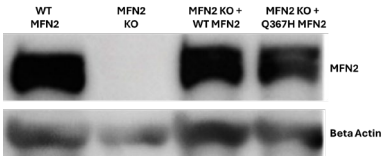
WT MFN2
MFN2 KO
MFN2 KO + WT MFN2
MFN2 KO + Q367H MFN2
MFN2
Beta Actin

C.

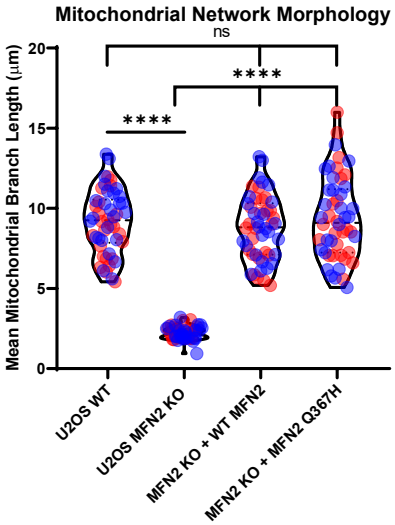
Mitochondrial Network Morphology
Mean Mitochondrial Branch Length (µm)
ns
****
****
U2OS WT
U2OS MFN2 KO
MFN2 KO + WT MFN2
MFN2 KO + MFN2 Q367H

D.

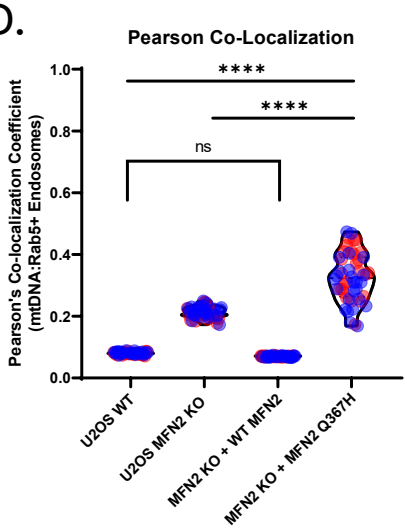
Pearson Co-Localization
Pearson's Co-localization Coefficient (mtDNA:Rab5+ Endosomes)
****
****
ns
U2OS WT
U2OS MFN2 KO
MFN2 KO + WT MFN2
MFN2 KO + MFN2 Q367H

Gene	Disease/ Inheritance pattern	Coding variant	Amino acid change	rsID	Max reported MAF	ClinVar	Zygosity	Polyphen 2 prediction	Mutation-taster prediction
MFN2	CMT neuropathy 2A; AD	c.1101G>C	p.Gln367His	rs373211062	0.00024	VUS, conflicting interpretations	Hetero-zygous	B	D
DYSF	LGMD 2B; AR	c.5180G>C	p.Gly1727Ala	rs146153532	1.16E-04	VUS	Hetero-zygous	P	D
SYNE1	EDMD 4; AD/AR	c.9934G>A	p.Asp3312Asn	rs147281213	2.33E-04	VUS	Hetero-zygous	D	D

AD=autosomal dominant; AR=autosomal recessive; B= benign; CMT=Charcot Marie Tooth; D=deleterious; EDMD=Emery Dreyfuss muscular dystrophy; LGMD=limb girdle muscular dystrophy; MAF=minor allele frequency; P=possibly tolerated; VUS=variant of uncertain significance.